

Thesis Title

A thesis submitted to the University of Manchester for the degree of
Doctor of Philosophy
in the Faculty of Science and Engineering

2022

Damian Crosby
Department of Mechanical, Aerospace and Civil Engineering

Contents

Contents	2
List of figures	4
List of tables	7
List of publications	8
List of abbreviations	9
Abstract	11
Declaration of originality	12
Copyright statement	13
Acknowledgements	14
1 A Literature Review of Terrestrial Robots with Robotic Tails and Their Functions	15
1.1 Introduction	15
1.1.1 Chapter Summary	15
1.2 Research Methodology	16
1.3 Tail Functions of Terrestrial Robots	16
1.3.1 Categorisation System	16
1.3.2 Examples from each Category	20
1.4 Discussion	32
1.4.1 Performance Comparison	32
1.4.2 Bio-Inspiration	33
1.4.3 Number of Segments	34
1.5 Conclusion	34
References	34
2 Creating a Configurable Payload for Instability Experiments	37
2.1 Introduction	37
2.1.1 Chapter Summary	37
2.2 Mathematical Design	38
2.2.1 Configuration Space	38
2.2.2 Test Point Sets	39

2.2.3	Search Methods	40
2.3	Implementation	42
2.3.1	Container Design	42
2.3.2	Selected Search Method	43
2.3.3	Material Selection	44
2.4	Results	45
2.4.1	Configuration Space	45
2.4.2	Test Points	45
2.5	Discussion & Conclusion	49
2.5.1	Future Work	49
2.5.2	Conclusion	50
	References	50
3	Investigating the use of a 2DOF Pendulum Tail for Compensating for Instability when Carrying a Payload	52
3.1	Introduction	52
3.1.1	Chapter Summary	52
3.2	Experiment Design	53
3.2.1	Base	54
3.2.2	Robot Arm	55
3.2.3	2 Degree of Freedom (DOF) Tail	55
3.2.4	Trajectory	55
3.3	Simulation	56
3.4	Experiments	56
3.4.1	Design	56
3.4.2	Results & Performance	56
3.5	Discussion and Conclusion	59
	References	59
	Appendices	61

List of figures

1.1	Flowchart of the publication selection process.	16
1.2	Abstract graphs of the different functions of the tail, with the magnitude representing some kind of change in the robot's position and/or orientation.	18
1.3	Tree diagram of all the categorisations found in the publications with accompanying visual diagrams.	19
1.4	Data from [1] showing the effects of a static and dynamic tail on maintaining robot heading in a trotting gait.	20
1.5	Image from [1] showing how the tail moves during the gait in order to correct for heading drift.	21
1.6	Simulation Data from [3] showing the how the body pitch would be reduced when accelerating or braking with an active tail.	21
1.7	Images from [3] showing the robot performing a rapid acceleration test with the tail.	22
1.8	Experimental Data from [3] showing the maximum acceleration achieved with and without an active tail.	22
1.9	Images from [6] showing the robot performing a turn with the tail.	22
1.10	Experimental Data from [5] (left) and [6] (right) showing the maximum lateral acceleration achieved with and without an active tail. Note the right graph manages similar results to the left graph.	23
1.11	Images of the robots in [7] (left) and [8] (right).	23
1.12	Data from [8] comparing the robot path on an XY plane for a 90° differential drive turn, open loop tail turn, and closed loop tail turn. Note the vastly increased sharpness of the turn when a tail is used.	24
1.13	Data from [7] showing the gain in yaw rate for various open loop tail trajectories and different frequencies and amplitudes.	24
1.14	Images from [8] showing the robot using its tail to make a turn.	24
1.15	Data from [9] showing the normalised change in Centre of Mass (COM) for a static and dynamic walk.	25
1.16	Data from [9] showing the trajectory of the COM and Zero Moment Point (ZMP) for a static and dynamic walk.	25
1.17	Video still of the TITRUS-III robot from [11].	26
1.18	Imagers from [10] showing how the tail or body deflect when hit by the wrecking ball, depending on if the tail is active.	26
1.19	Data from [10] showing the difference in hip displacement between a fixed and controlled tail.	27

1.20	Data from [12] showing the optimal spring constant for maximising jumping height.	27
1.21	Images from [12] showing the motion of the tail during a jump.	28
1.22	Data from [13] showing the increase in forward velocity and/or reduction in body pitch for the different tail lengths and masses. Note that a) and c) correspond to a 35° tail amplitude, while b) and d) are a 65° amplitude.	28
1.23	Images from [13] showing the motion of the body and tail over a single stride cycle.	29
1.24	Images from [14] showing the a single stride for the robot, and an image of the robot just before landing.	30
1.25	Diagrams from [16] outlining the two reorientation experiments.	31
1.26	Images from [16] showing the wall reorientation experiment.	31
1.27	Images from [16] showing the slope reorientation experiment.	31
1.28	Diagram from [16] showing the obstacle impact test.	32
1.29	Images from [16] showing the slope obstacle impact test without a tail, with a static tail, and with a dynamic tail with closed loop feedback.	32
1.30	Graphs of various publications that varied tail design or control, normalised to the best performing variation (= 100%) for each metric, for a unitless comparison.	33
2.1	Concept drawing of the configurable payload.	38
2.2	Various temperature cooling profiles for simulated annealing, assuming 1000 steps.	42
2.3	Schematic of the container, including body and lid.	43
2.4	Simulated annealing output for the target $\begin{bmatrix} 1.5 & 0.001 & 0.001 & 0.001 \end{bmatrix}$ with $\alpha = 0.997$ and even weighting $w_m, w_r = 0.25$ for 4.3×10^4 steps.	44
2.5	Masses for each set of eight 35 mm cubes of the configurable payload for each of the four materials, with the mean mass \bar{x} and standard deviation σ of each set.	44
2.6	Scatter graph of all 62969 unique mass and COM vectors.	45
2.7	Mass and COM coordinates for each test point set.	46
2.8	Example configuration space for the new configurable payload design, where $z = 0$	49
2.9	Renders of a concept design for the new configurable payload, with a single rod and dual rod configuration.	50
2.10	Diagram on the COM dynamics of a fluid filled container. If the container is disturbed, a standing wave forms inside the container which causes the COM to oscillate.	50
3.1	Free body diagram of the static test setup.	54
3.2	System diagram of the static rig.	54
3.3	Exploded schematic of the base of the static rig, with important components labelled and clamping points marked.	55

3.4	Trajectory sequence of the robot arm and payload.	55
3.5	Simulation block diagram.	56
3.6	Block diagram of the control system.	57
3.7	Graph of the mean Center of Pressure (COP) during the <i>carry</i> phase of the experiment	58
3.8	Resonant frequency of the tail calculated from accelerometer data captured during an impact with a steel hammer. The left graph is the accelerometer data, and the right graph is the real part from a real Discrete Fourier Transform (DFT) on the data.	58
3.9	59

List of tables

1.1	Table of animals referenced in publications.	34
2.1	The materials chosen for the cubes.	45
2.2	Table of the vectors of \mathcal{E} , excluding the mass-limited element.	45
2.3	Table of the target and actual vectors for \mathcal{C} , \mathcal{B} and the mass limited element of \mathcal{E} with the L2 norm error. * notation indicates “don’t care” and is excluded from the search algorithm.	46
2.4	Table of all test point configurations,	47
2.5	48
2.6	48

List of publications

Publications go here.

List of abbreviations

AUJ Actuated Universal Joint

2D Two Dimensional

3D Three Dimensional

COM Centre of Mass

DLS Damped Least Squares

DOF Degree of Freedom

PID Proportional Integral Derivative

PI Proportional Integral

PD Proportional Derivative

SHTP Sensor Hub Transport Protocol

MSB Most Significant Bit

LSB Least Significant Bit

I²C Inter-Integrated Circuit

SPI Serial Peripheral Interface

UART Universal Asynchronous Receiver-Transmitter

DIO Digital Input/Output

IMU Inertial Measurement Unit

GOOP Graphical Object Oriented Programming

CS Chip Select

DFT Discrete Fourier Transform

CPG Central Pattern Generator

ODE Ordinary Differential Equation

GRF Ground Reaction Force

ZMP Zero Moment Point

RMS Root Mean Square

COP Center of Pressure

ADC Analog to Digital Converter

NI National Instruments

PC Personal Computer

Abstract

This is abstract text.

Declaration of originality

I hereby confirm that no portion of the work referred to in the thesis has been submitted in support of an application for another degree or qualification of this or any other university or other institute of learning.

Copyright statement

- i The author of this thesis (including any appendices and/or schedules to this thesis) owns certain copyright or related rights in it (the “Copyright”) and s/he has given The University of Manchester certain rights to use such Copyright, including for administrative purposes.
- ii Copies of this thesis, either in full or in extracts and whether in hard or electronic copy, may be made *only* in accordance with the Copyright, Designs and Patents Act 1988 (as amended) and regulations issued under it or, where appropriate, in accordance with licensing agreements which the University has from time to time. This page must form part of any such copies made.
- iii The ownership of certain Copyright, patents, designs, trademarks and other intellectual property (the “Intellectual Property”) and any reproductions of copyright works in the thesis, for example graphs and tables (“Reproductions”), which may be described in this thesis, may not be owned by the author and may be owned by third parties. Such Intellectual Property and Reproductions cannot and must not be made available for use without the prior written permission of the owner(s) of the relevant Intellectual Property and/or Reproductions.
- iv Further information on the conditions under which disclosure, publication and commercialisation of this thesis, the Copyright and any Intellectual Property and/or Reproductions described in it may take place is available in the University IP Policy (see <http://documents.manchester.ac.uk/DocuInfo.aspx?DocID=24420>), in any relevant Thesis restriction declarations deposited in the University Library, The University Library’s regulations (see <http://www.library.manchester.ac.uk/about/regulations/>) and in The University’s policy on Presentation of Theses.

Acknowledgements

Acknowledgements go here.

Chapter 1

A Literature Review of Terrestrial Robots with Robotic Tails and Their Functions

1.1 Introduction

The field of terrestrial robots with robotic tails is incredibly diverse, reflecting the many functions of tails in the animal kingdom. Even discounting tails used for fluid dynamics (swimming and flying robots), and focusing only on robots that use their tail during “terrestrial” locomotion (broadly defined as when a robot is moving along a contiguous surface, or jumping from one surface to another surface), there are many applications of robotic tails. In order to make sense of the state of the field, an abstract categorisation system is considered based on the environment the robot is in when the tail is active, the specific action the robot is taking to move itself in space, and what the specific function of the tail is with respect to the robot dynamics. Using this categorisation system, various examples are explored from a set of research articles selected using specific keywords. From this, conclusions can be derived about the general design and operation of robotic tails, which can be used to influence and guide the research covered in chapters 3.

1.1.1 Chapter Summary

In this chapter, a research methodology is described that produces a collection of relevant publications in the field of terrestrial mobile robots with tails. A categorisation system is developed based on the function of the tail and how it contributes to the robot’s dynamics. In each category, selected publications are then summarised with accompanying figures from the source material. In the discussion, broader findings about the qualities of the robot tails found in the literature are explained, which include what performance comparisons were made between different tail designs, motions, or control methods within the same publication for the same tail function, any bio-inspiration the publication took from the animal kingdom, be it through direct performance comparsion, or loose “inspiration”, and finally whether multiple segments confer any performance advantage in specific tail applications.

1.2 Research Methodology

Using three online publication repositories, *IEEE Xplore*, *Scopus* and *Web of Science*, a search query was conducted to find relevant publications. The query was tailored to include all publications with **tail*** or **appendage** in the title along with **robot*** (* indicates a wild-card suffix), but to exclude publications that concerned swimming, water walking, or flying robots, as using a tail as a rudder to influence fluid dynamics was outside of the scope of the research. Further exclusions were added upon experimentation with the query in order to remove false positives in areas such as chemistry (as molecules are often described as having “tails”) or medicine (as it did not pertain to mobile robots and usually concerned biological structures such as proteins and cells). The date range was set from January 1980 to December 2018 to exclude outdated publications. The exact queries for each repository can be found in table ??.

As a result XX publications were discovered. After duplicates were removed and after screening abstracts and full texts, a total of XX unique publications were selected for inclusion. A flowchart of this process can be found in figure 1.1.

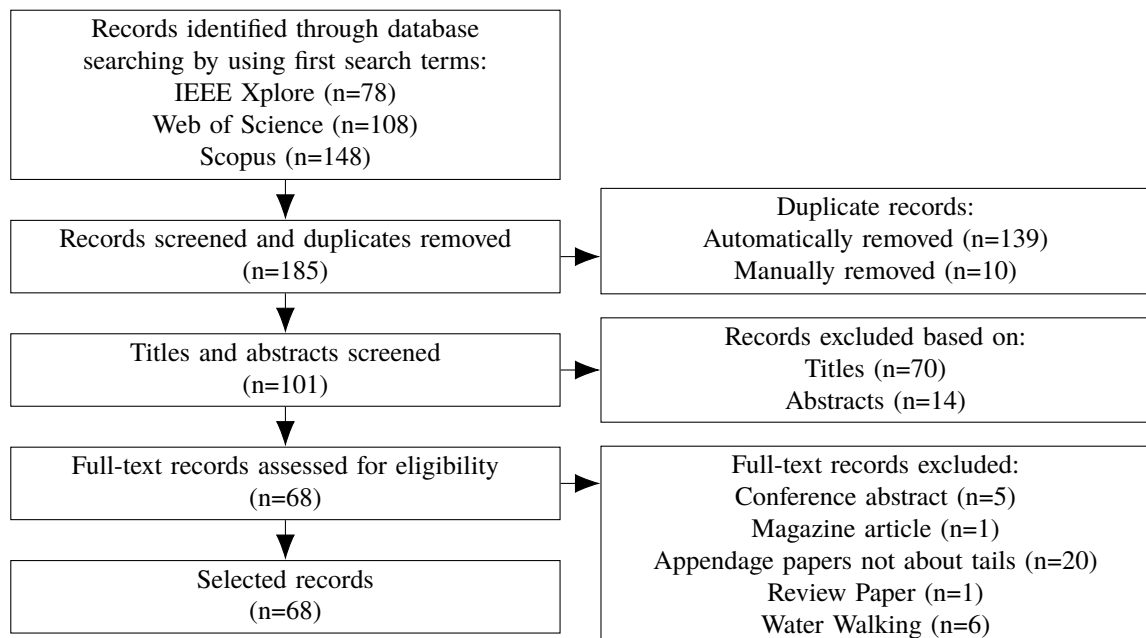


Figure 1.1: Flowchart of the publication selection process.

1.3 Tail Functions of Terrestrial Robots

1.3.1 Categorisation System

The resulting publications represented a wide array of different robot designs and multiple forms of locomotion. Therefore, a simple categorisation system was required in order to better understand the majority of the functions of these tails. After careful analysis of the literature, two questions could be asked that provided common answers:

1. Is the robot on the ground, in the air or transitioning between those states when the tail is active?
2. What precisely is the robot doing when the tail is active?
3. What does the tail do to the dynamics of the robot (i.e. what would happen if there *wasn't* a tail present)?

Each question can then assign a tiered category to a publication based on the answer, the three tiers named *Environment*, *Action* and *Function*.

1. **Environment:** The general domain the robotic system is operating in when the tail is active. From the reviewed literature, three categories have been created:
 - *Terrestrial:* A robot with an active tail when the robot is touching a surface, such as a robot driving along the ground.
 - *Aerial:* A robot with an active tail when the robot is in free space, such as a robot which *has jumped* into the air, or is falling off a ledge.
 - *Transition:* A robot with an active tail when the robot is just about to transition from between the two previous environments, such as a robot *just about* to jump into the air.
2. **Action:** The specific action the robot is performing when the tail is active. Most actions are unique to each environment, except for *hopping*.
 - *Straight:* A robot travelling across a surface maintaining its direction of travel.
 - *Accelerating:* A robot changing its velocity in the direction of travel across a surface. In the literature, this was a robot coming to complete stop, and starting from stationary.
 - *Turning:* A robot changing its direction of travel across a surface, such as a robot turning a corner.
 - *Balancing:* A robot undergoing external disturbances while travelling across a surface, typically due to adverse terrain, such as a robot navigating a rough and uneven surface without falling over.
 - *Hopping:* A robot executing a sequence of periodic jumps in order to travel across a surface, similar to the method of locomotion of a Kangaroo.
 - *Jumping/Falling:* A robot executing isolated non-periodic jumps, falling off a ledge or launching off a ramp, typically to transition from one surface to another at a different altitude and/or orientation.
3. **Function:** The purpose of the tail when the robot is performing the action. These categories usually apply to multiple actions.

- *Stability*: The tail is used to *Maintain* some aspect of the robot's position and/or orientation from the start of the action.
- *Initiation*: The tail is used to *Change* some aspect of the robot's position and/or orientation from the start of the action.
- *Amplification*: The tail is used to *Amplify* the effects of an action by other parts of the robot (such as the legs) which changes the position and/or orientation.

For example, a robot with a tail that helps it increase its apex when hopping, is in the *Transition* environment as it is about to transition from being on the ground to in the air when the tail is active. The robot itself locomotes by hopping, so it is performing a *Hopping* action, and since without the tail the robot would still be capable of hopping, but would not have such a tall apex, the tail can be considered to be performing *Amplification* of the robot's existing capabilities. Overall, this results in the categorisation *Transition* → *Hopping* → *Amplification*.

Another example is a robot with a tail that prevents it from falling over on rough terrain. The robot is in the *Terrestrial* environment as it is on the ground when the tail is active. The robot itself is performing a *Balancing* action as it is trying to remain upright during locomotion, and since without the tail the robot would fall over, the tail can be considered to be maintaining the *Stability* of the robot. Overall, this results in the categorisation *Terrestrial* → *Balancing* → *Stability*.

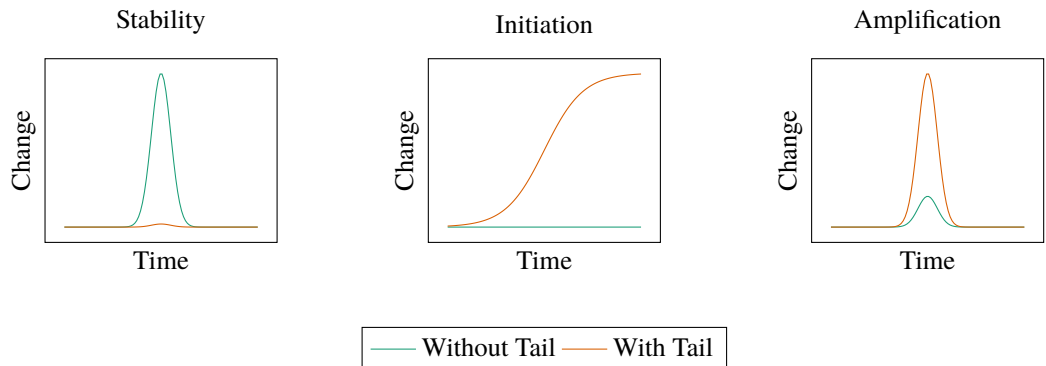


Figure 1.2: Abstract graphs of the different functions of the tail, with the magnitude representing some kind of change in the robot's position and/or orientation.

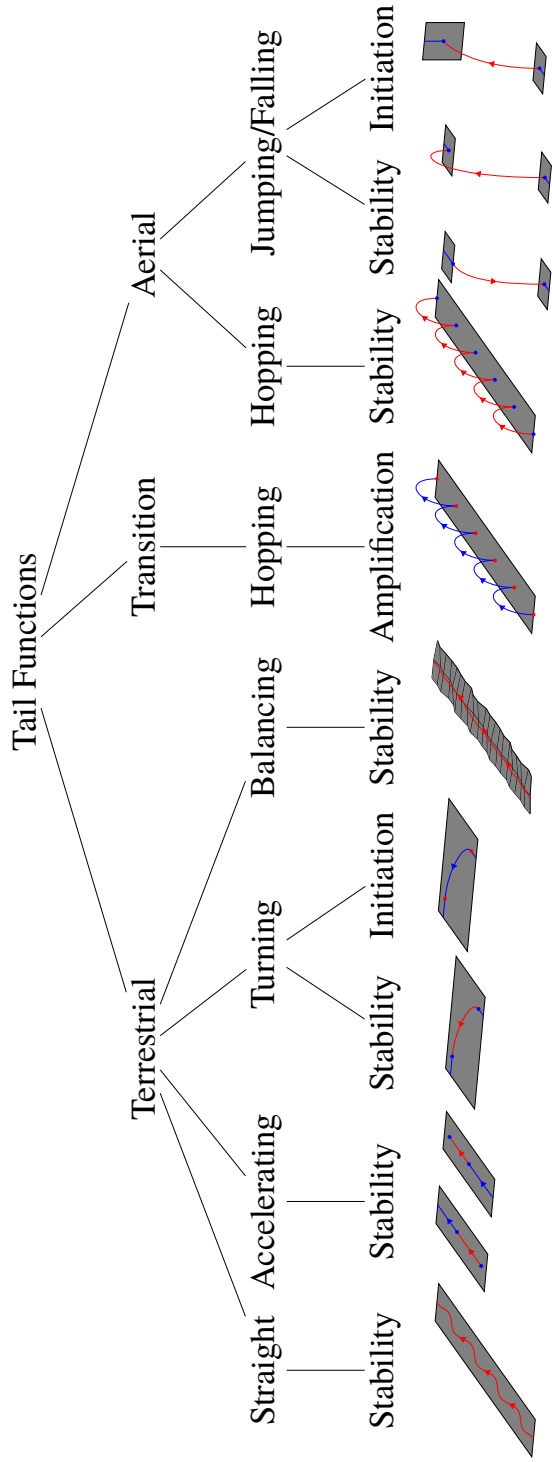


Figure 1.3: Tree diagram of all the categorisations found in the publications with accompanying visual diagrams.

1.3.2 Examples from each Category

1.3.2.1 Terrestrial → Straight → Stability

[1] uses a quadrupedal robot with a gait controlled by a Central Pattern Generator (CPG), an open loop control concept based on neural networks found in the spinal chords of vertebrates and invertebrate thoracic ganglia [2]. A CPG in robotics is typically constructed from a network of oscillators represented by a system of Ordinary Differential Equation (ODE), which accepts the input of another oscillator as a parameter in the system. By chaining these together, complex synchronised trajectories can be generated for multiple actuators in robot locomotion.

Upon initial experiments with a trotting locomotion with no active tail, the robot would not maintain a set heading, it would instead slowly begin to drift in a circle. Visual observations noted that the robot would topple onto its front left leg that was in “swing” phase (lifted off the ground), and it would drag on the ground until in “stance” phase. This resulted in a difference between the Ground Reaction Force (GRF) of the left and right feet which caused the drift in locomotion path.

By implementing a swinging tail that imparted an opposing torque to the direction of the topple, the differences between the left and right GRF were reduced, and the robot could maintain its heading, as can be seen in figure 1.4.

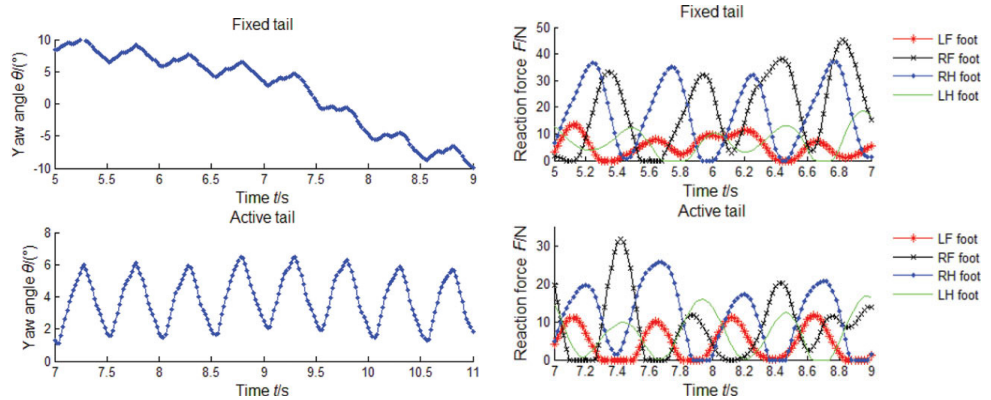


Figure 1.4: Data from [1] showing the effects of a static and dynamic tail on maintaining robot heading in a trotting gait.

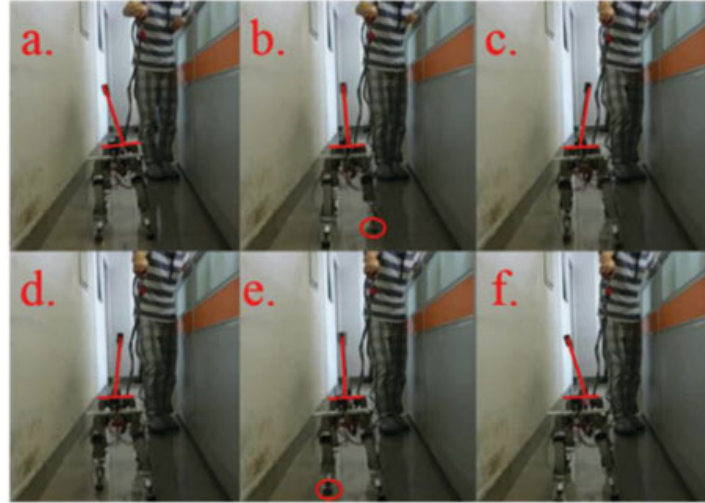


Figure 1.5: Image from [1] showing how the tail moves during the gait in order to correct for heading drift.

1.3.2.2 *Terrestrial → Accelerating → Stability*

[3] used inspiration from the Cheetah (*Acinonyx jubatus*) to improve the acceleration and braking capabilities of a wheeled robot. The research is based on findings from [4], which shows that quadruped acceleration and deceleration in the animal kingdom is limited by their ability to constrain body pitch to prevent toppling over. It can be considered analogous to a motorcycle: accelerate too fast and the vehicle will “pop a wheelie” and potentially flip backwards, decelerate too fast and the opposite may occur.

Using a combined state feedback and Proportional Integral (PI) controller based on the angular position of the tail, and the angular velocity of the tail and body, the researchers were able to increase the acceleration and braking capabilities of the robot by using the tail to generate an opposing torque to the direction of body pitch, as can be seen in figure 1.8. This was verified by running a series of experiments, increasing the acceleration/braking magnitude until the robot failed to complete the test by toppling over.

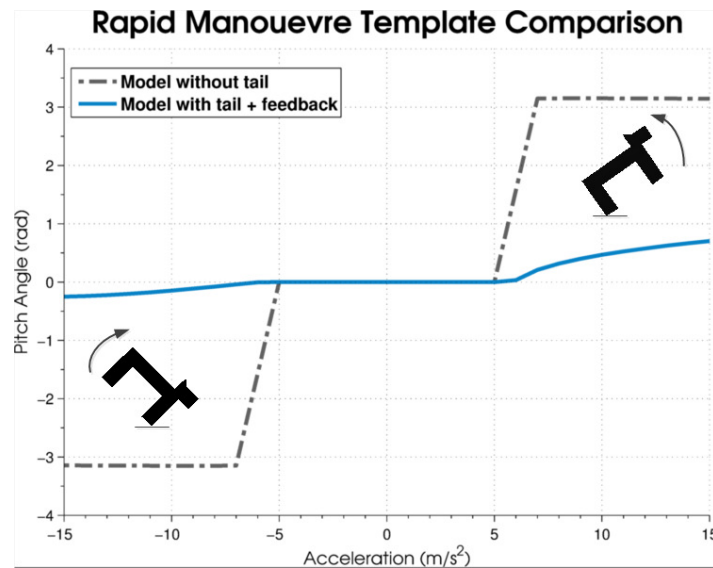


Figure 1.6: Simulation Data from [3] showing the how the body pitch would be reduced when accelerating or braking with an active tail.



Figure 1.7: Images from [3] showing the robot performing a rapid acceleration test with the tail.

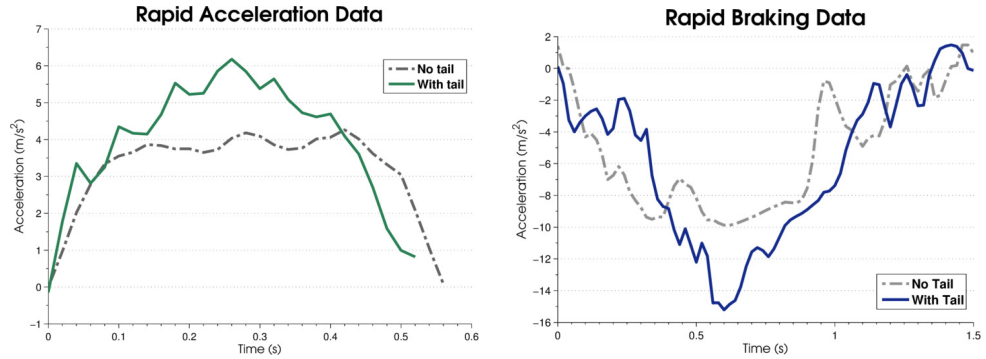


Figure 1.8: Experimental Data from [3] showing the maximum acceleration achieved with and without an active tail.

1.3.2.3 *Terrestrial → Turning → Stability*

[5], [6] took similar inspiration from the Cheetah to allow for tighter turns by allowing greater lateral acceleration. [5] swings the tail out in a single motion in the direction of the turn, producing an opposing torque to the centrifugal force that would otherwise topple the robot during the turn. In contrast, [6] moves the tail constantly in a conical motion, the direction of rotation in the direction of the turn. This also produces an opposing torque in the same fashion, but was not limited in duration, as in the first strategy the tail would eventually contact the ground. This allowed for turns of longer duration to be stabilised.

The control system and experimental procedures were similar to those in [3].

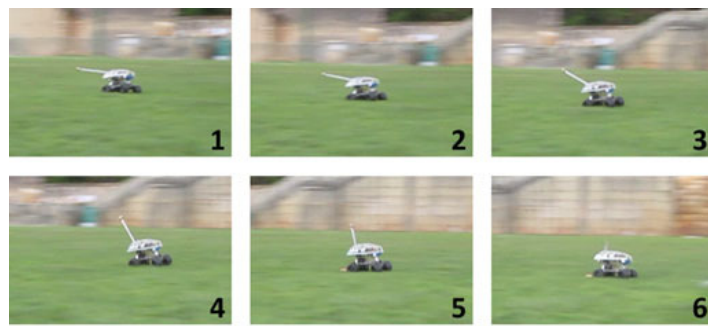


Figure 1.9: Images from [6] showing the robot performing a turn with the tail.

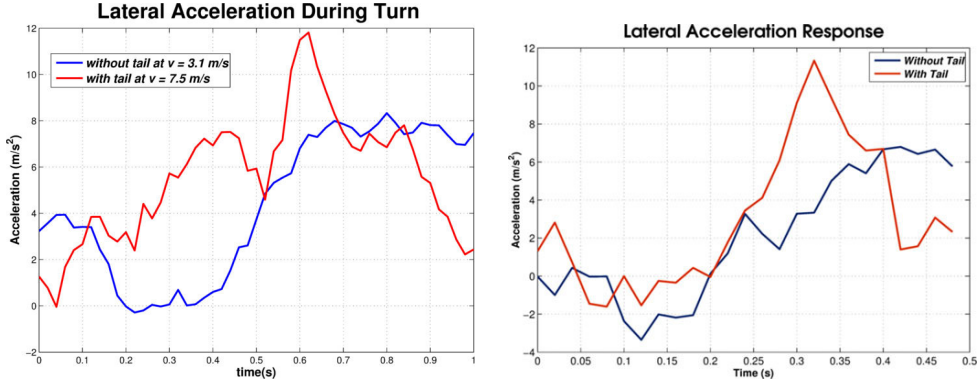


Figure 1.10: Experimental Data from [5] (left) and [6] (right) showing the maximum lateral acceleration achieved with and without an active tail. Note the right graph manages similar results to the left graph.

1.3.2.4 *Terrestrial → Turning → Initiation*

[7], [8] both use similar robot designs, insect like robots that locomote using 6-8 pairs of small legs (in this case [7] used a robot with eight legs, and [8] used six legs). Both robots are designed to be very light (52 g in [7] and 46 g in [8]) so the legs have a low friction force with the ground. A suitably weighted tail, when swung out in a horizontal motion, can overcome this friction force and impart enough torque to rotate the body of the robot to a new heading.

[8] compared an open and closed loop response of the tail, while [7] only compared open loop tail responses at different frequencies and amplitudes, as can be seen in figure 1.13.

Both experiments were able to greatly increase the turning rate of the robot over a turn using a differential drive, at 360° s^{-1} for [8] and 400° s^{-1} for [7].

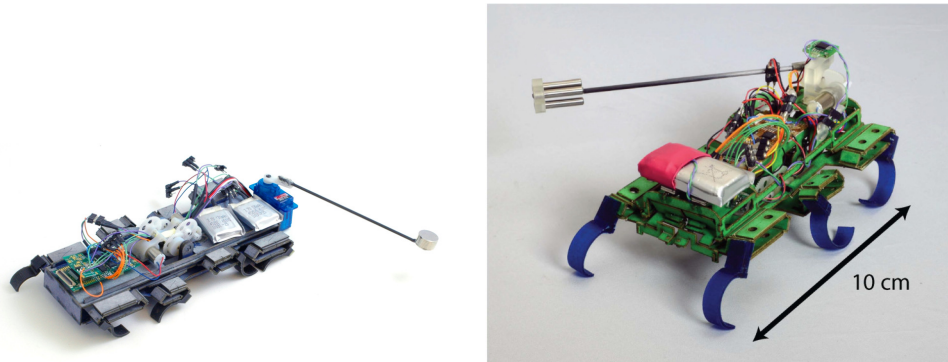


Figure 1.11: Images of the robots in [7] (left) and [8] (right).

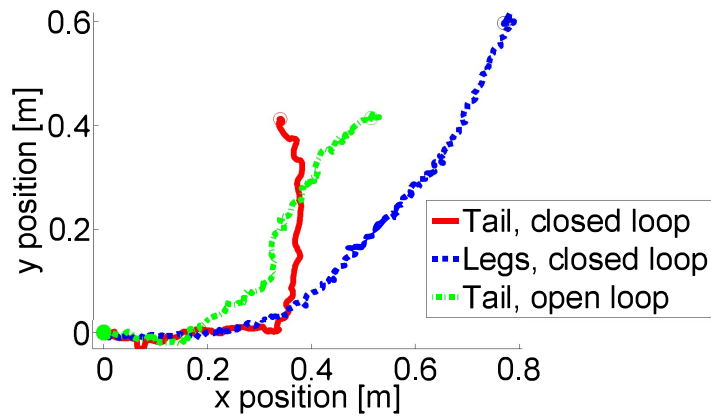


Figure 1.12: Data from [8] comparing the robot path on an XY plane for a 90° differential drive turn, open loop tail turn, and closed loop tail turn. Note the vastly increased sharpness of the turn when a tail is used.

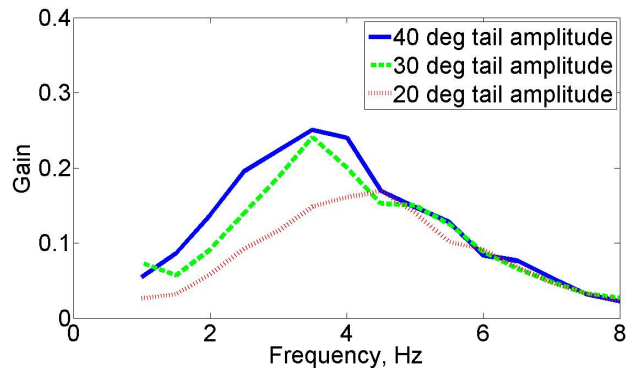


Figure 1.13: Data from [7] showing the gain in yaw rate for various open loop tail trajectories and different frequencies and amplitudes.



Figure 1.14: Images from [8] showing the robot using its tail to make a turn.

1.3.2.5 Terrestrial → Balancing → Stability

The forces that may cause the robot to topple over when balancing can result from both *internal* forces: robot design or joint inertia when moving at high speed, and *external* forces: uneven terrain or impact. [9] is concerned with internal forces, whereas [10] is concerned with external forces.

[9] used a dinosaur like bipedal robot with a long neck and tail. The neck and tail then swung from side to side during the gait, maintaining the stability of the robot. Two experiments were conducted using different strategies for maintaining stability. The “static” method swung the neck and tail in a trapezoidal motion in order to keep the COM within the area of the current foot on the ground. The “dynamic” method calculated the ZMP of the robot and instead constrained that to keep it within the are of the foot. This resulted in a smaller motion of the neck and tail which enabled a faster gait.

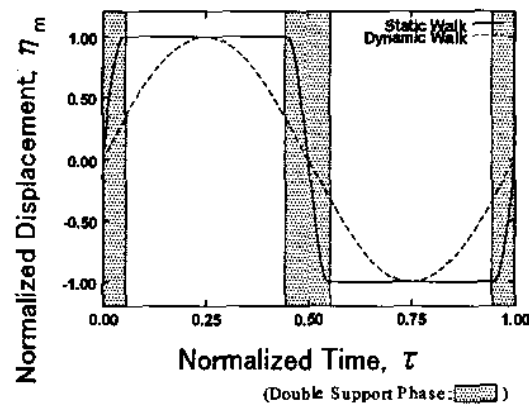


Figure 1.15: Data from [9] showing the normalised change in COM for a static and dynamic walk.

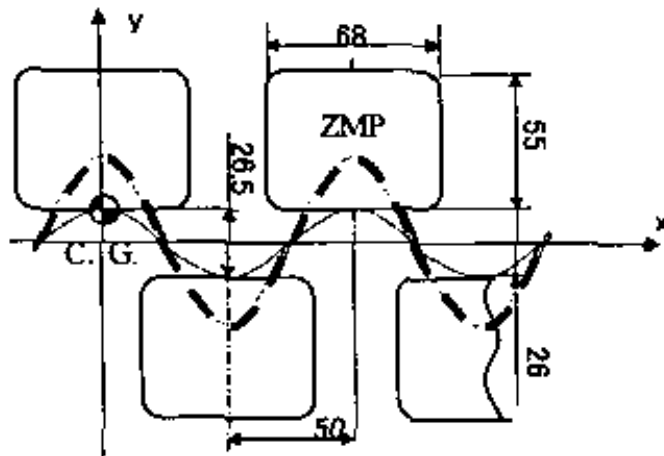


Figure 1.16: Data from [9] showing the trajectory of the COM and ZMP for a static and dynamic walk.

[10] uses a quadrupedal robot closely modelled on a Cheetah which is hit in the torso by a “wrecking ball” to simulate a disturbance. In the control experiment the weighted tail remains static, in the active tail experiment the tail responds in an open loop trajectory when triggered by an accelerometer that sensed the impact. The active tail experiment was able to

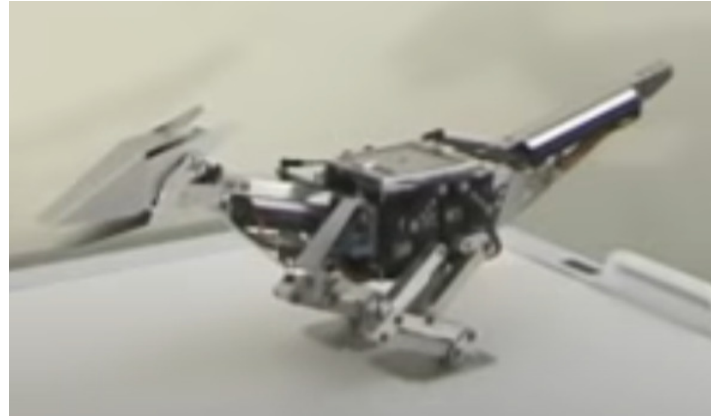


Figure 1.17: Video still of the TITRUS-III robot from [11].

significantly reduce the hip displacement after impact, as can be seen in figure 1.19.

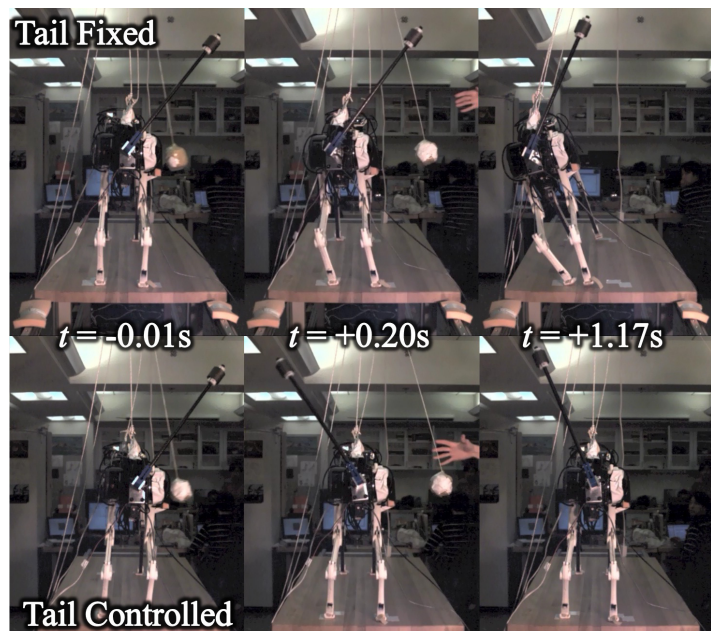


Figure 1.18: Imagers from [10] showing how the tail or body deflect when hit by the wrecking ball, depending on if the tail is active.

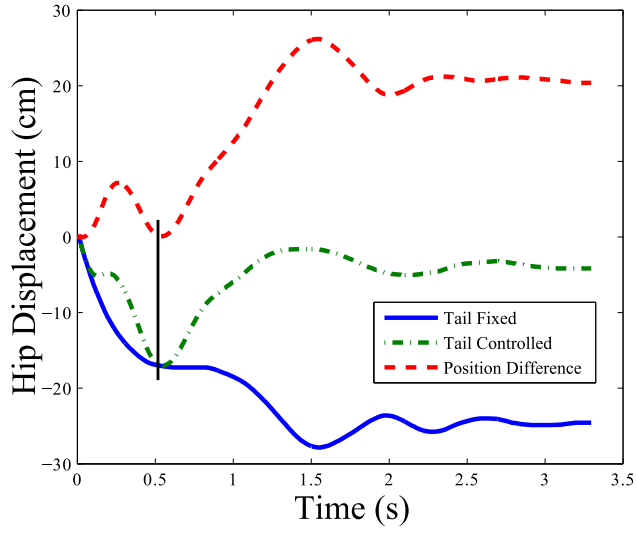


Figure 1.19: Data from [10] showing the difference in hip displacement between a fixed and controlled tail.

1.3.2.6 *Transition → Hopping → Amplification*

[12], [13] both use a tail to increase the magnitude of a hopping gait. [12] increases the *height* of the hop, while [13] increases the *length*.

[12] uses a bipedal robot with a long, flexible tail. The tail consists of six segments, connected together by passive spring revolute joints. The only active joint connects the tail assembly to the robot body. This creates a “whip-like” motion in the tail when the joint is actuated. By experimenting with different spring constants, an optimum value that maximises jumping height can be found, as can be seen in figure 1.22. Results showed a significant increase in jump height, 256 mm over 240 mm for a model with a rigid tail, and 210 mm for a mode with an inactive tail, demonstrating the superiority of a flexible tail in this application.

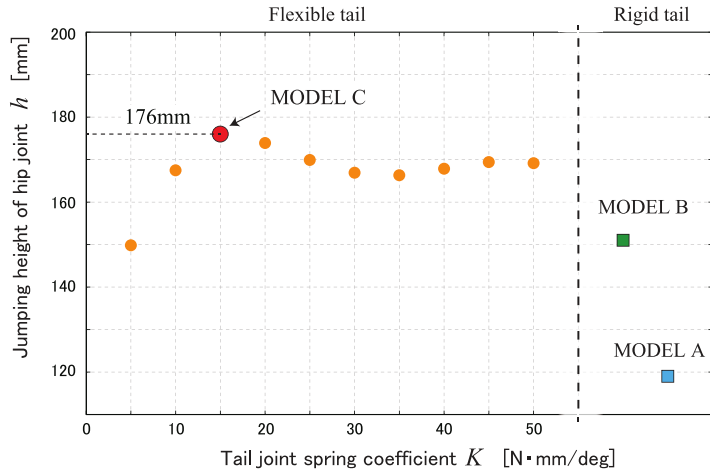


Figure 1.20: Data from [12] showing the optimal spring constant for maximising jumping height.

[13] uses a quadrupedal robot that locomotes in a galloping motion. By using a weighted tail in an open loop trajectory, the robot is about to increase its forward velocity while also

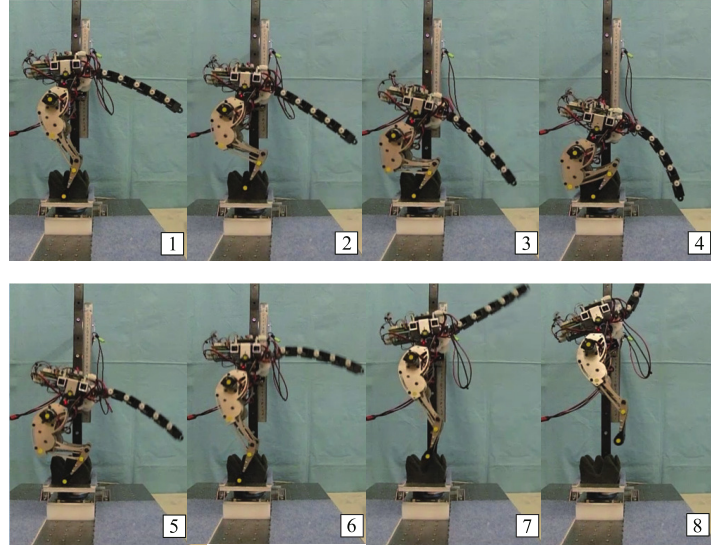


Figure 1.21: Images from [12] showing the motion of the tail during a jump.

reducing body pitch. Two different tail lengths and masses were used for experiments, a long, light tail (31 g/168 mm), and a short heavy tail (53 g/128 mm). Different open loop amplitudes, 35° and 65° , were also used for each experiment. Results showed an increase in forward velocity and reduction in body pitch, with the best forward velocity of 0.558 m s^{-1} from the short, heavy tail at 35° , and the best reduction in body pitch per stride of 4.6° from the long, light tail at 65° . These results compared to a forward velocity of 0.479 m s^{-1} and body pitch per stride of 8.5° for a fixed “passive” tail.

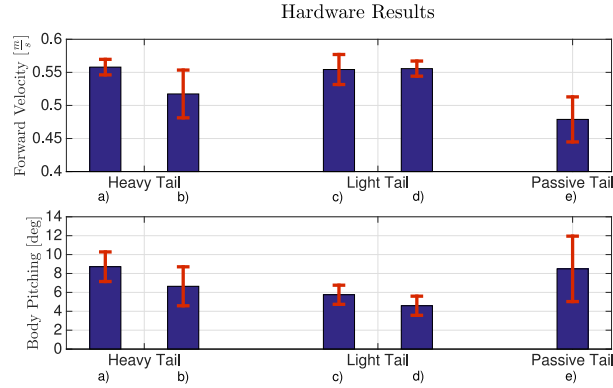


Figure 1.22: Data from [13] showing the increase in forward velocity and/or reduction in body pitch for the different tail lengths and masses. Note that a) and c) correspond to a 35° tail amplitude, while b) and d) are a 65° amplitude.

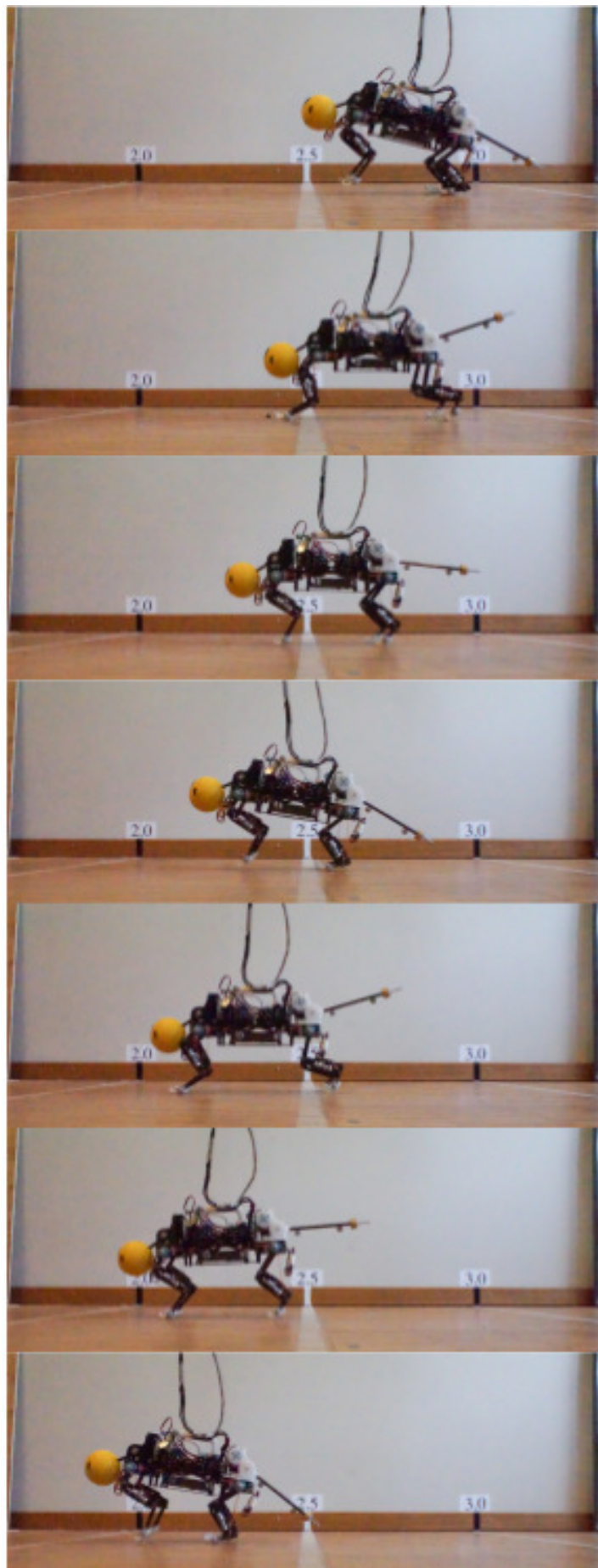


Figure 1.23: Images from [13] showing the motion of the body and tail over a single stride cycle.

1.3.2.7 Aerial → Hopping → Stability

[13] also used the tail to reduce body pitch, which prevents the robot from falling over forward when hopping. [14] also used a kangaroo like robot with a tail to also decrease body pitch, in both an open and closed loop tail trajectory. The open loop tail was able to reduce the body pitch range to 5.17° and Root Mean Square (RMS) error to 1.17° , and the closed loop tail to 4.49° with an RMS of 0.96° , as compared to 7.18° with an RMS of 2.24° for a stationary tail (in this case, *range* refers to the difference between the maximum and minimum pitch angle during the hop).

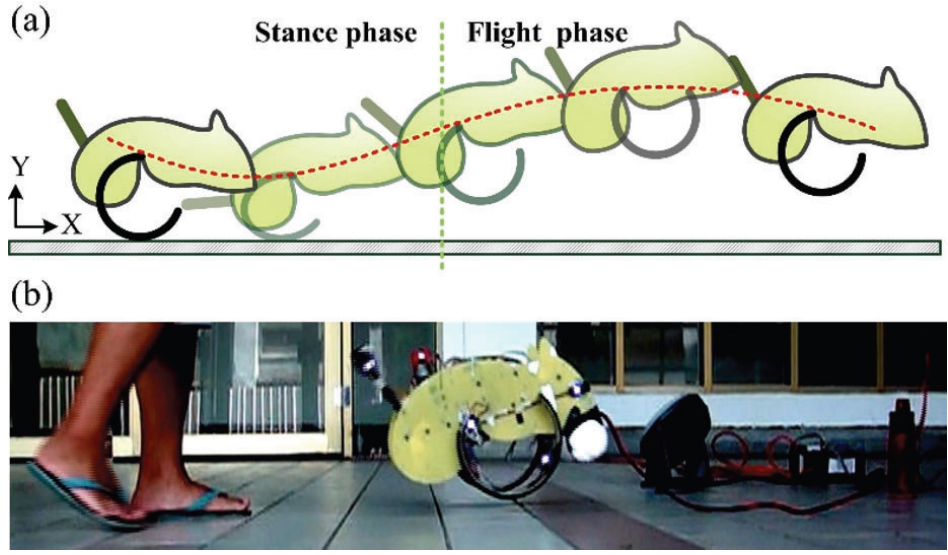


Figure 1.24: Images from [14] showing the a single stride for the robot, and an image of the robot just before landing.

[15] also developed a bipedal robot with a 2 DOF tail that was used to maintain a stable hopping motion.

1.3.2.8 Aerial → Jumping/Falling → Initiation

[16] uses a wheeled robot with a weighted tail to reorient the robot in mid-air. Two experiments are carried out to this end, where the robot is released from a vertical position on a wall and attempts to land horizontally, and where the robot drives off a ledge and attempts to land on a 45° sloped surface. The tail used a Proportional Derivative (PD) feedback controller with body orientation as input. In both experiments, the robot was able to successfully reorient itself.

[17] used a robot that was able to wheel itself to a specific position, then rotate itself using the tail as an appendage into a different orientation which allowed it to launch itself into the air. Then once in the air it would use the tail itself to orient itself back so it landed on its wheels.

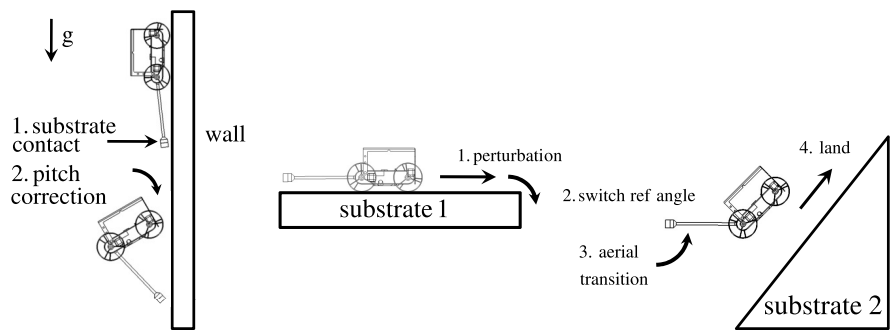


Figure 1.25: Diagrams from [16] outlining the two reorientation experiments.

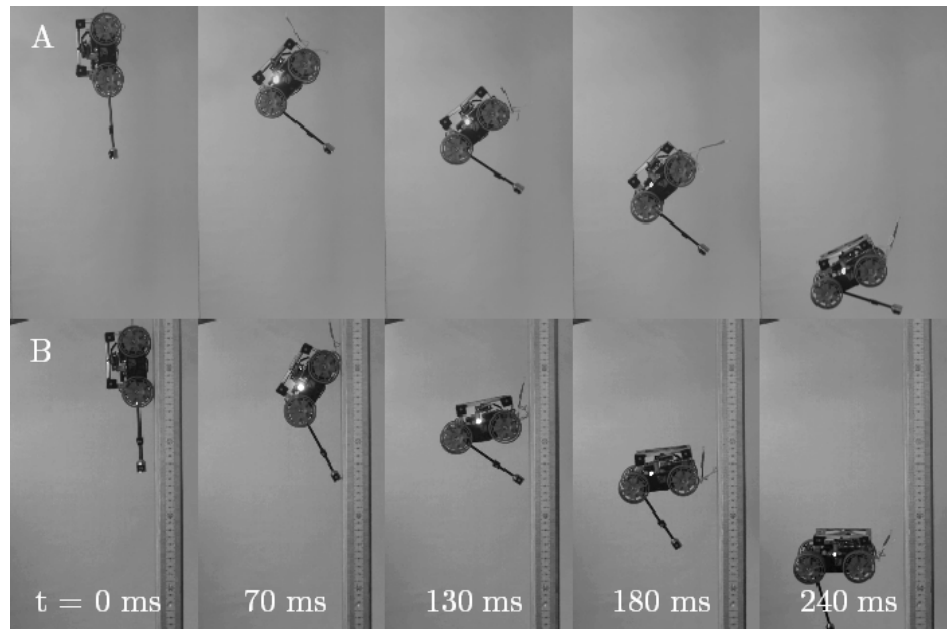


Figure 1.26: Images from [16] showing the wall reorientation experiment.



Figure 1.27: Images from [16] showing the slope reorientation experiment.

1.3.2.9 Aerial → Jumping/Falling → Stability

[16] also conducted an experiment where the robot would hit a small obstacle when driving along a surface, causing it to go airborne. Experiments were conducted without a tail, with a static tail, and with a closed loop controlled tail.

[18] had a hexapod robot that was able to remain upright when running off a ledge.

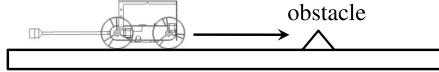


Figure 1.28: Diagram from [16] showing the obstacle impact test.

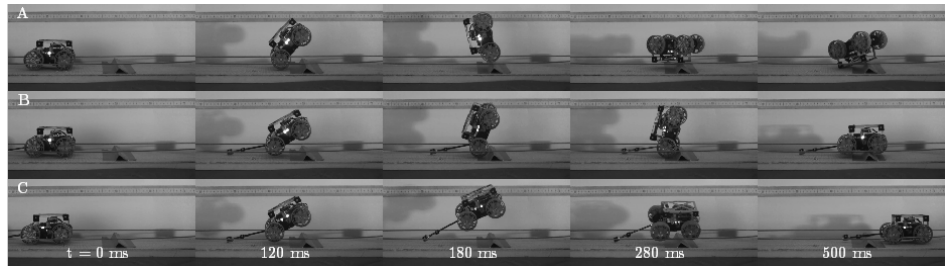


Figure 1.29: Images from [16] showing the slope obstacle impact test without a tail, with a static tail, and with a dynamic tail with closed loop feedback.

1.4 Discussion

Many tails were designed to be multi functional, as evidenced by experiments of different functions within the same publication, and/or multiple publications that included the same robot.

1.4.1 Performance Comparison

A number of publications varied their tail design [12], [13] or control system [14], [17], and were able to record improvements in performance for various metrics. Figure 1.30 shows selected publications performance comparisons, normalised to the best performing variation for each metric, for a unitless comparison. For control systems, the more complex and advanced the better the performance, understandable since a publication is unlikely to test a more complex control system unless there is high confidence in a performance improvement. For tail design, the picture is more complex. While [12] demonstrates a clear improvement in performance for a flexible tail, a more complex design, [13] shows how tail design can result in trade-offs between different metrics, with different tail designs being superior. However, it is possible to see the *Long Light Tail (65°)* is the optimal choice, since reduction in *Forward Velocity* is slight, but the reduction in *Body Pitch* (a negative metric, where a larger value is worse) is significant, assuming both metrics are equally weighted.



Figure 1.30: Graphs of various publications that varied tail design or control, normalised to the best performing variation (= 100%) for each metric, for a unitless comparison.

1.4.2 Bio-Inspiration

used data from animal tails as a comparison to their own experimental data, clearly showing a link between biological tail functions and robot tail functions. mention an animal tails in as part of the introduction to their research, but do not make any performance comparisons, instead considering their form and function as inspiration for the design and implementation of the robot tail. The following animal tails were considered in experimental mobile robot publications:

The Kangaroo tail was found in publications for robots in the *Aerial → Hopping → Stability* and *Transition → Hopping → Amplification* category. The Cheetah tail was found in publications for robots in the

Animal	Referenced In
Kangaroo	
Cheetah	
Agama Lizard	
Velociraptor	

Table 1.1: Table of animals referenced in publications.

1.4.3 Number of Segments

Only a couple of publications [12], [19] experimented with mobile robots using tails with multiple segments. Other publications only experimented with multi-segment tails in isolation, some with speculation on future inclusion in a mobile robot. As mentioned in subsections 1.4.1 and 1.3.2.6, [12] managed to achieve a mm improvement in jump height using a sprung flexible tail instead of a rigid one. The relative paucity of experimental multi-segment tails could be explained due to complexities in dynamics and control, as even in [12] only the first joint was actuated and the rest passively spring-loaded, resulting in a simple design and control system. If the future research of some isolated multi-segment tail experiments is realised, then more data will be available.

1.5 Conclusion

Based on the review undertaken here, the field of robotic tails in terrestrial locomotion is very diverse and varied. Tails appear to be used for a number of wide ranging applications, some with bio-inspiration and some without. By far the most common design for a tail is a rigid single segment with 1-2 DOF, unlike in the animal kingdom where multi-segment tails are the norm. Therefore going forward, it was prudent to choose this kind of tail for later research, at least for initial experiments. However, a multi-segment approach may still yield advantages, and a simulation study for the primary research application is discussed in chapter ??.

References

- [1] Z. Xiuli, G. Jiaqing, and Y. Yanan, “Effects of head and tail as swinging appendages on the dynamic walking performance of a quadruped robot,” *Robotica*, vol. 34, no. 12, pp. 2878–2891, 2016.
doi: 10.1017/S0263574716000011.
- [2] A. J. Ijspeert, “Central pattern generators for locomotion control in animals and robots: A review,” *Neural networks*, vol. 21, no. 4, pp. 642–653, 2008.

- [3] A. Patel and M. Braae,
“Rapid acceleration and braking: Inspirations from the cheetah’s tail,”
in *Robotics and Automation (ICRA), 2014 IEEE International Conference on*, IEEE, 2014, pp. 793–799. doi: 10.1109/ICRA.2014.6906945.
- [4] S. B. Williams, H. Tan, J. R. Usherwood, and A. M. Wilson, “Pitch then power: Limitations to acceleration in quadrupeds,”
Biology letters, vol. 5, no. 5, pp. 610–613, 2009.
- [5] A. Patel and M. Braae,
“Rapid turning at high-speed: Inspirations from the cheetah’s tail,” in *Intelligent Robots and Systems (IROS), 2013 IEEE/RSJ International Conference on*, IEEE, 2013, pp. 5506–5511. doi: 10.1109/IROS.2013.6697154.
- [6] A. Patel and E. Boje, “On the conical motion of a two-degree-of-freedom tail inspired by the cheetah,”
IEEE Transactions on Robotics, vol. 31, no. 6, pp. 1555–1560, 2015.
doi: 10.1109/TRO.2015.2495004.
- [7] A. O. Pullin, N. J. Kohut, D. Zarrouk, and R. S. Fearing,
“Dynamic turning of 13 cm robot comparing tail and differential drive,”
in *Robotics and Automation (ICRA), 2012 IEEE International Conference on*, IEEE, 2012, pp. 5086–5093. doi: 10.1109/ICRA.2012.6225261.
- [8] N. J. Kohut, A. O. Pullin, D. W. Haldane, D. Zarrouk, and R. S. Fearing, “Precise dynamic turning of a 10 cm legged robot on a low friction surface using a tail,”
in *Robotics and Automation (ICRA), 2013 IEEE International Conference on*, IEEE, 2013, pp. 3299–3306. doi: 10.1109/ICRA.2013.6631037.
- [9] K. Takita, T. Katayama, and S. Hirose, “Development of dinosaur-like robot titrus-motion control of the head and tail of miniature robot titrus-iii,”
in *SICE 2002. Proceedings of the 41st SICE Annual Conference*, IEEE, vol. 5, 2002, pp. 2984–2989. doi: 10.1109/SICE.2002.1195580.
- [10] R. Briggs, J.-W. Lee, M. Haberland, and S.-B. Kim,
“Tails in biomimetic design: Analysis, simulation, and experiment,” in *Intelligent Robots and Systems (IROS), 2012 IEEE/RSJ International Conference on*, IEEE, 2012, pp. 1473–1480. doi: 10.1109/IROS.2012.6386240.
- [11] “The dinosaur-like biped robot titrus-iii,” YouTube. (2010),
[Online]. Available: <https://www.youtube.com/watch?v=GxVv4WNlXMA>.

- [12] R. Sato, S. Hashimoto, A. Ming, and M. Shimojo, “Development of a flexible tail for legged robot,” in *Mechatronics and Automation (ICMA), 2016 IEEE International Conference on*, IEEE, 2016, pp. 683–688. doi: 10.1109/ICMA.2016.7558645.
- [13] S. W. Heim, M. Ajallooeian, P. Eckert, M. Vespiagnani, and A. J. Ijspeert, “On designing an active tail for legged robots: Simplifying control via decoupling of control objectives,” *Industrial Robot: An International Journal*, vol. 43, no. 3, pp. 338–346, 2016. doi: 10.1108/IR-10-2015-0190.
- [14] L. Guan-Horng, L. Hou-Yi, L. Huai-Yu, C. Shao-Tuan, and L. Pei-Chun, “A bio-inspired hopping kangaroo robot with an active tail,” *Journal of Bionic Engineering*, vol. 11, no. 4, pp. 541–555, 2014. doi: 10.1016/S1672-6529(14)60066-4.
- [15] J. An, T. Chung, C. H. D. Lo, C. Ma, X. Chu, and K. S. Au, “Development of a bipedal hopping robot with morphable inertial tail for agile locomotion,” in *2020 8th IEEE RAS/EMBS International Conference for Biomedical Robotics and Biomechatronics (BioRob)*, IEEE, 2020, pp. 132–139.
- [16] E. Chang-Siu, T. Libby, M. Tomizuka, and R. J. Full, “A lizard-inspired active tail enables rapid maneuvers and dynamic stabilization in a terrestrial robot,” in *Intelligent Robots and Systems (IROS), 2011 IEEE/RSJ International Conference on*, IEEE, 2011, pp. 1887–1894. doi: 10.1109/IROS.2011.6094658.
- [17] Z. Jianguo, Z. Tianyu, X. Ning, M. W. Mutka, and X. Li, “Msu tailbot: Controlling aerial maneuver of a miniature-tailed jumping robot,” *IEEE/ASME Transactions on Mechatronics*, vol. 20, no. 6, pp. 2903–2914, 2015. doi: 10.1109/TMECH.2015.2411513.
- [18] T. Libby, A. M. Johnson, E. Chang-Siu, R. J. Full, and D. E. Koditschek, “Comparative design, scaling, and control of appendages for inertial reorientation,” *IEEE Transactions on Robotics*, vol. 32, no. 6, pp. 1380–1398, 2016. doi: 10.1109/TRO.2016.2597316.
- [19] B. Simon, R. Sato, J.-Y. Choley, and A. Ming, “Development of a bio-inspired flexible tail system,” in *2018 12th France-Japan and 10th Europe-Asia Congress on Mechatronics*, IEEE, 2018, pp. 230–235.

Chapter 2

Creating a Configurable Payload for Instability Experiments

2.1 Introduction

In order to generate a diverse set of test data for the experiments in chapter 3, a configurable payload was conceived, an object that could be configured to have a wide range of masses and COM. A series of test points can then be generated which have a specific mass and COM, and a matching algorithm can be used to find the configuration that mostly closely matches these parameters. The experiments can then be run with each of these test points to generate the test data.

The payload consists of a matrix of cubes of various materials packed tightly into a Three Dimensional (3D) printed container. The cubes are designed to be changed after each experimental run to alter the mass and COM of the payload. A lid on the container prevents the cubes from falling out during the experiment, and the exterior design of the box may accommodate additional features to improving the handling of the payload by the robot arm.

The test points can then be generated by considering the *Configuration Space* of the payload design, i.e. how many permutations can be generated given a $n \times n \times n$ matrix of cubes, where each cube can be a number of different materials. The mass and COM can then be calculated for each permutation, taking into account the material density and mass and COM of the container. “Extrema” test points can then be found simply by finding the permutation with the maximum or minimum mass and COM, or combination thereof. Depending on the number of permutations, a search method can then be used that accepts an arbitrary mass and COM as a target, and finds the nearest permutation to that target for other test point sets.

2.1.1 Chapter Summary

In this chapter, an abstract mathematical model of the configurable payload is conceived, which the mass and COM of a specific permutation of the payload can be derived from. Then three separate sets of “test points” are considered to cover a wide range of the available configuration space within the chosen robot arms performance limits, using a com-

bined mass and COM vector as a target which finds the closest permutation using a search function, or extrema which maps onto a specific permutation. For target test points, two search methods are examined, one brute force method for small permutation sets and one for larger sets where a brute force method would be computationally intractable. Then the chosen implementation is described, including the number of block materials, the number of blocks, the size and design of the container and the chosen search method. The results of this implementation for all test point sets are then tabulated and graphed. In the discussion, the limitations of the mass and COM range are considered, and potential designs to expand the range and scope of the experiments in chapter 3 are conceived, specifically improving the range of the COM and simulating dynamic loads.

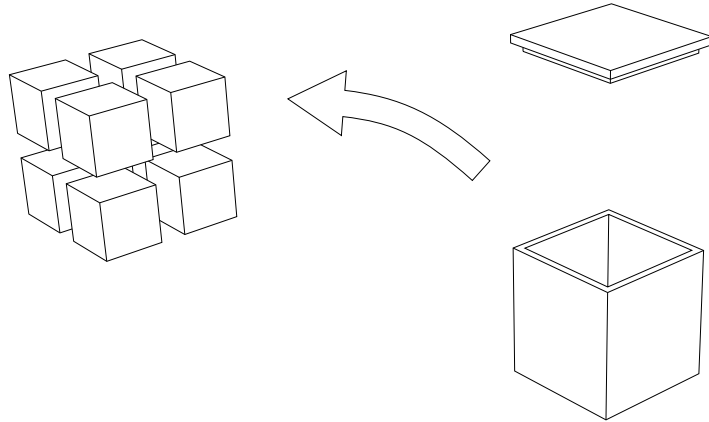


Figure 2.1: Concept drawing of the configurable payload.

2.2 Mathematical Design

2.2.1 Configuration Space

Firstly, consider a positive real set of material densities $\mathcal{P} \in \mathbb{R}^+$, each element the density (in kg m^{-3}) of a material to be used:

$$\mathcal{P} = \{\rho_1, \rho_2 \dots \rho_n \mid \rho_i > 0\} \quad (2.1)$$

Each permutation can then be defined as an $n \times n \times n$ matrix \mathbf{C} , such that each element is an element of \mathcal{P} , where n^3 is the number of cubes in the matrix:

$$\mathbf{C} = (c_{ijk}) \in \mathbb{R}^{n^n} \mid (c_{ijk}) \in \mathcal{P} \quad (2.2)$$

\mathcal{Z} can then be defined as the set of all permutations of \mathbf{C} .

To calculate the mass of the permutation, take the sum of all the cube densities multiplied by their volume a^3 , where a is the cube edge length, plus the container mass m_c :

$$M(\mathbf{C}) = \left(\sum_{i=1}^n \sum_{j=1}^n \sum_{k=1}^n c_{ijk} a^3 \right) + m_c \quad (2.3)$$

To calculate the COM, take the sum of each cube mass multiplied by its position relative to the centroid of the center cube (c_{222}), which can be calculated from the cube indexes ijk , plus the container COM \mathbf{r}_c if non-zero:

$$R(\mathbf{C}) = \frac{\left(\sum_{i=1}^n \sum_{j=1}^n \sum_{k=1}^n c_{ijk} a^4 \left([i \ j \ k] - n + 1 \right) \right) + \mathbf{r}_c}{M(\mathbf{C})} \quad (2.4)$$

The *configuration space* \mathcal{Y} can then be considered as a set of \mathbb{R}^4 vectors containing the target mass and COM concatenated as $[m_i \ \mathbf{r}_i]$ of each element. As such, \mathcal{Y} is a codomain of \mathcal{X} , such that $H : \mathcal{X} \mapsto \mathcal{Y}$ where map function H is $[M(\mathbf{C}) \ R(\mathbf{C})]$

2.2.2 Test Point Sets

Test points can either be derived from subsets of \mathcal{X} defined by logical expressions, or the nearest neighbours of \mathcal{Y} from a target mass and COM concatenated into a vector as in H , found by a *search method* (see subsection ??).

2.2.2.1 Extrema Set (\mathcal{E})

The extrema set is designed to test the extremas of the space of \mathcal{Z} for both $M(\mathcal{Z})$ and $R(\mathcal{Z})$. The extrema set is defined from a set of logical constraints. The first two constraints of the set find the maximum and minimum values of the payload mass using $M(\mathcal{Z})$, and the next four constraints use the payload COM using $M(\mathcal{C})$ to get the maximum and minimum values of the x and y component of the COM. Finally, the last four constraints define the diagonal maximum and minimum values where the COM components match $x = y$ or $x = -y$.

$$\mathcal{E} = \left\{ \mathbf{x} \in \mathcal{Z} \mid \begin{array}{l} M(\mathbf{x}) = \max \{M(\mathcal{Z})\} \\ M(\mathbf{x}) = \min \{M(\mathcal{Z})\} \\ R(\mathbf{x})_x = \max \{R(\mathcal{Z})_x\} \\ R(\mathbf{x})_x = \min \{R(\mathcal{Z})_x\} \\ R(\mathbf{x})_y = \max \{R(\mathcal{Z})_y\} \\ R(\mathbf{x})_y = \min \{R(\mathcal{Z})_y\} \\ R(\mathbf{x})_x = \max \{R(\mathcal{Z})_x\} \wedge R(\mathbf{x})_x = R(\mathbf{x})_y \\ R(\mathbf{x})_x = \min \{R(\mathcal{Z})_x\} \wedge R(\mathbf{x})_x = R(\mathbf{x})_y \\ R(\mathbf{x})_x = \max \{R(\mathcal{Z})_x\} \wedge R(\mathbf{x})_x = -R(\mathbf{x})_y \\ R(\mathbf{x})_x = \min \{R(\mathcal{Z})_x\} \wedge R(\mathbf{x})_x = -R(\mathbf{x})_y \end{array} \right\} \quad (2.5)$$

Mass Limited \mathcal{E} When this set was generated, it was found that $M(\mathcal{E}_1)$ was greater than the chosen robot arm in chapter 3 could safely lift (2.0 kg [1]). Experiment trials also found the grippers were failing to consistently hold masses lower than this for long enough to complete the experiment. Therefore, $M(\mathbf{x}) = \max\{M(\mathcal{Z})\}$ in \mathcal{E} was changed to $\begin{bmatrix} m_{max} & 0 & 0 & 0 \end{bmatrix}$ where m_{max} is the mass limit that the robot arm can lift reliably. One of the search methods described in section ?? can then be used to find the nearest point in configuration space.

2.2.2.2 Cube Set (\mathcal{C})

The cube set is defined by the vertices of a cube of size b centred around the COM origin $\begin{bmatrix} 0 & 0 & 0 \end{bmatrix}$.

$$\mathcal{C} = \left\{ \mathbf{x} \in \mathcal{C} \mid \begin{bmatrix} \pm \frac{b}{2} & \pm \frac{b}{2} & \pm \frac{b}{2} \end{bmatrix} = \mathbf{x} \right\} \quad (2.6)$$

2.2.2.3 Balanced Set (\mathcal{B})

The balanced set is defined by q points in \mathcal{C} subject to the constraint $R(\mathbf{x})_x = 0 \wedge R(\mathbf{x})_y = 0$. This can be defined as a “balanced” set as the COM x and y components are both zero. The points are evenly spaced between the maximum and minimum mass as defined in section ??.

$$\begin{aligned} m_r &= \frac{\max\{M(\mathcal{Z})\} - \min\{M(\mathcal{Z})\}}{q+1} \\ \mathbf{z} &= \begin{bmatrix} m_r & 2m_r & \cdots & qm_r \end{bmatrix} \\ \mathcal{B} &= \left\{ \mathbf{x} \in \mathcal{C} \mid z_i = \mathbf{x} \wedge R(\mathbf{x})_x = 0 \wedge R(\mathbf{x})_y = 0 \right\} \end{aligned} \quad (2.7)$$

2.2.3 Search Methods

When considering a viable search method given a target, the cardinality of \mathcal{X} is important to consider. It is defined as $|\mathcal{X}| = |\mathcal{P}|^{n^3}$ which increases super exponentially with n . For example, when $|\mathcal{P}| = 4$, $n = 2$ results in 65536 permutations and $n = 3$ results in approximately 1.8×10^{16} permutations. It’s very clear that when $n > 2$ for non-trivial cardinalities of \mathcal{P} , any kind of brute-force method is not computationally tractable. Therefore, a brute-force nearest neighbour method (see subsection 2.2.3.2) would be suitable for when $n = 2$, and a heuristic search method such as simulated annealing (see subsection 2.2.3.1) method would be suitable for when $n > 2$.

2.2.3.1 Multiobjective Simulated Annealing

Simulated annealing [2] is a modification to a gradient descent optimisation that allows the algorithm the chance to “jump out” of local minima early on (even though the approxima-

tion becomes temporarily worse). However, as the number of remaining steps decreases, that probability becomes smaller, becoming more and more like gradient descent. First, like any gradient descent algorithm, two things need to be generated, the initial configuration \mathbf{C}_0 , which can be random or manually selected, and the function $\mathcal{N}(\mathbf{C})$ which creates a set of all the “neighbours” of \mathbf{C} . In this case, this can be defined as the subset of \mathcal{X} where the difference between \mathbf{C} and an element of $\mathcal{N}(\mathbf{C})$ is one and only one $c_{ijk} \neq c'_{ijk}$:

$$\mathcal{N}(\mathbf{C}) = \{x \subset \mathcal{X} \mid \exists! (c_{ijk} \neq c'_{ijk})\} \quad (2.8)$$

Then the simulated annealing function can be described as follows:

1. Set \mathbf{C} to the initial permutation \mathbf{C}_0 .
2. For each of the optimisation steps:
 - (a) Set the temperature value t with function $T\left(\frac{k_{max}}{k}\right)$ which takes into account the number of remaining steps.
 - (b) Set \mathbf{C}_{new} as a random element from the set of all neighbours of \mathbf{C} as defined by $\mathcal{N}(\mathbf{C})$.
 - (c) Use acceptance probability function $P(E(\mathbf{C}), E(\mathbf{C}_{new}), t)$ where $E(\mathbf{C})$ is the energy function.
 - (d) Compare that value with a random uniformly distributed real number between 0 and 1. If greater than or equal to, then replace \mathbf{C} with \mathbf{C}_{new} . Otherwise, keep it the same.
 - (e) Repeat with \mathbf{C} until there are no remaining steps.
3. Return the approximated permutation \mathbf{C} .

```

 $\mathbf{C} = \mathbf{C}_0$ 
for  $k \leftarrow 1, k_{max}$  do
   $t = T\left(\frac{k_{max}}{k}\right)$ 
   $\mathbf{C}_{new} = \mathcal{N}(\mathbf{C}) \xleftarrow{R} x$ 
  if  $P(E(\mathbf{C}), E(\mathbf{C}_{new}), t) \geq x \sim U([0, 1])$  then
     $\mathbf{C} = \mathbf{C}_{new}$ 
  end if
end for
return  $\mathbf{C}$ 

```

Energy Function Simulated annealing can also be adapted for multi-objective optimisation [3], so it is possible to generate test points that approximate a desired mass and COM simultaneously.

Cooling Function The function which controls the probability of exiting local minima (known as the *temperature*) is known as the *cooling function*. This function can be any function which monotonically decreases (except in adaptive simulated annealing where it is dependant on the accuracy of the current approximation). Different functions will result in a different cooling profile, generally decreasing quickly in the first few steps, and then slowing down after that.

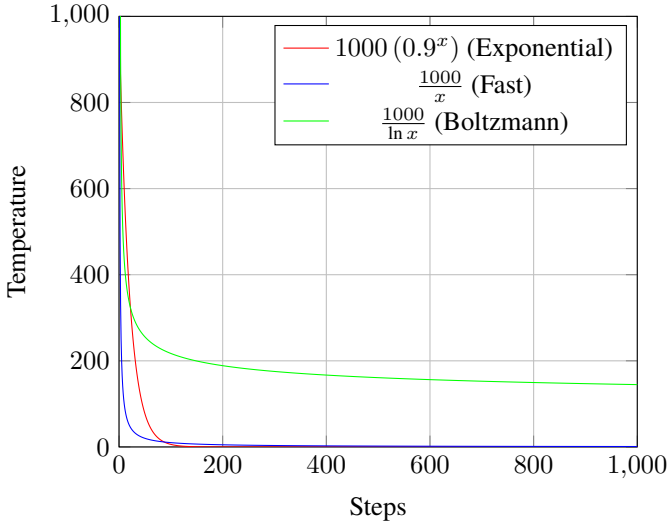


Figure 2.2: Various temperature cooling profiles for simulated annealing, assuming 1000 steps.

2.2.3.2 Nearest Neighbour

If \mathcal{X} is suitably small, then a brute-force method can be used which is guaranteed to find the nearest element to the target within a finite time. This can be done by calculating the L2 norms between the target vector t and all the elements of \mathcal{Y} and finding the minimum. If there are several elements in the domain of \mathcal{X} , then one is chosen at random from this set.

$$NN(t, \mathcal{X}) = \min \{ \|t - x\|_2 \mid \forall x \in \mathcal{Z}\} \quad (2.9)$$

2.3 Implementation

2.3.1 Container Design

The internal width of the container was chosen to be 76 mm, which combined with a wall width of 5 mm gives an overall width of 81 mm. Therefore, each cube would be $\frac{75}{n}$ mm in size, to allow for fitting clearance. For additional resiliency, the base would be an additional 4 mm, giving the container an overall height of 90 mm with the lid (not including gripper guides).

Two sides of the container were made of a textured pattern designed to enhance grip when picked up by the robot arm. The other two sides had small windows centred around each

cube, for permutation verification during the experiments in chapter ???. The lid of the container had a small notch to allow for it to be levered off in case of a tight fit, and guides to ensure the robot arm grippers would pick up the container in the same location each time, ensuring experiment repeatability.

The cube was 3D printed in **PLA!** (**PLA!**) with an 80% fill density. This gave it a total mass of 0 kg which provides the value for m_c . By design, the COM of the container would be 0 mm in both the x and y direction, to within a reasonable manufacturing tolerance. Due to the minimal contribution of the container to the total mass, this was a suitable assumption.

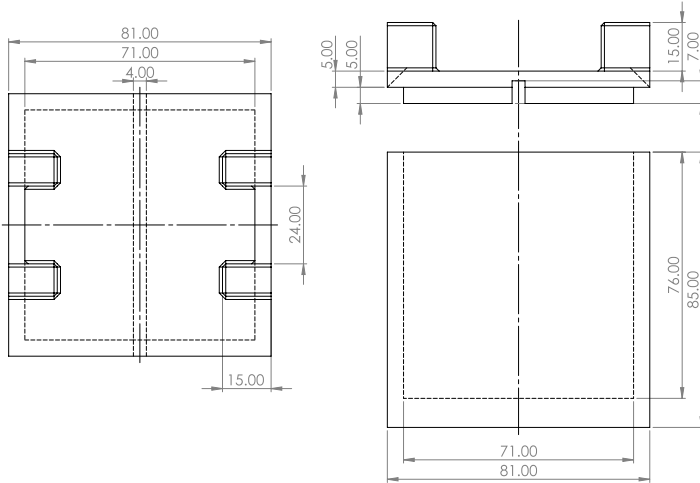


Figure 2.3: Schematic of the container, including body and lid.

2.3.2 Selected Search Method

Initially an $n = 3$ configuration was used with the acceptance probability function *Rule M* from [3]. This is a weighted blend of two other algorithms defined in the paper, *Rule P* and *Rule W* with a weighting coefficient $\alpha \in (0, 1) \subset \mathbb{R}$. There is also a weighting vector for each element of the test point $\mathbf{w} \in \mathbb{R}^4 \mid w_i \in (0, 1)$.

$$P(\mathbf{x}, \mathbf{y}, \mathbf{w}, t) = \underbrace{\alpha \prod_{i=1}^m \min \left\{ 1, e^{\frac{w_i(x_i - y_i)}{t}} \right\}}_{\text{Rule P}} + (1 - \alpha) \underbrace{\min \left\{ 1, \max_{i=1, \dots, m} \left\{ 1, e^{\frac{w_i(x_i - y_i)}{t}} \right\} \right\}}_{\text{Rule W}} \quad (2.10)$$

Unfortunately it was difficult to find a stable and consistent result even after a long time running the algorithm.

Therefore as an alternative, the $n = 2$ configuration was used, with larger cubes to compensate.

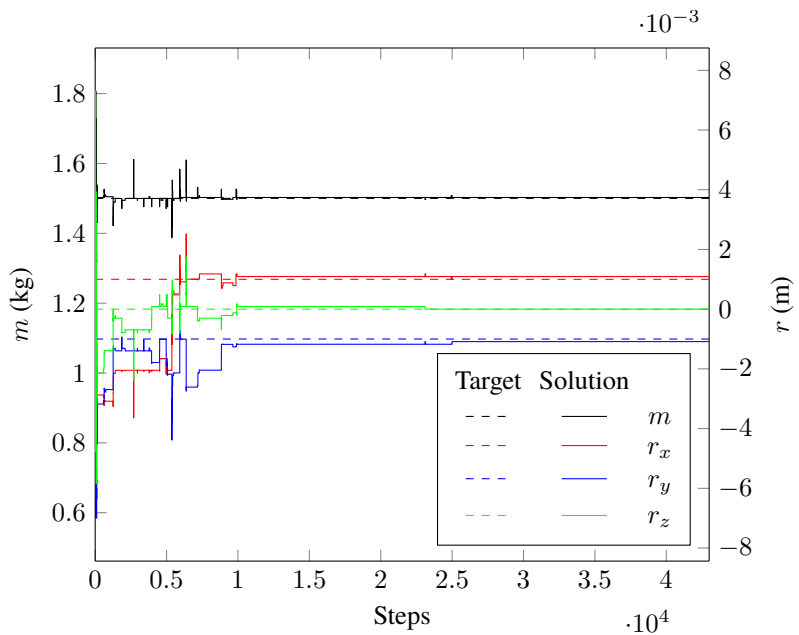


Figure 2.4: Simulated annealing output for the target $[1.5 \quad 0.001 \quad 0.001 \quad 0.001]$ with $\alpha = 0.997$ and even weighting $w_m, w_r = 0.25$ for 4.3×10^4 steps.

2.3.3 Material Selection

In order to produce a reasonably wide and dense configuration space, four materials: *wood*, *plastic*, *aluminium* and *steel*, were chosen. More dense materials, such as nickel and lead, were rejected due to difficulty sourcing stock of the correct size, or issues with machining. Initially estimated densities were used in order to test the simulated annealing algorithm, but after the cubes were manufactured, it was possible to get an average density based on the measured mass of each cube as seen in figure 2.5, given a cube size of 35 mm. Table 2.1 lists the exact kind of material used, and its calculated density. These differ from many stated values available from other sources such as online material databases, likely due to small discrepancies in cube size due to manufacturing tolerances and variability in material composition (particularly for wood since the blocks required sanding in order to fit in the container, and due to the less precise properties of natural materials).

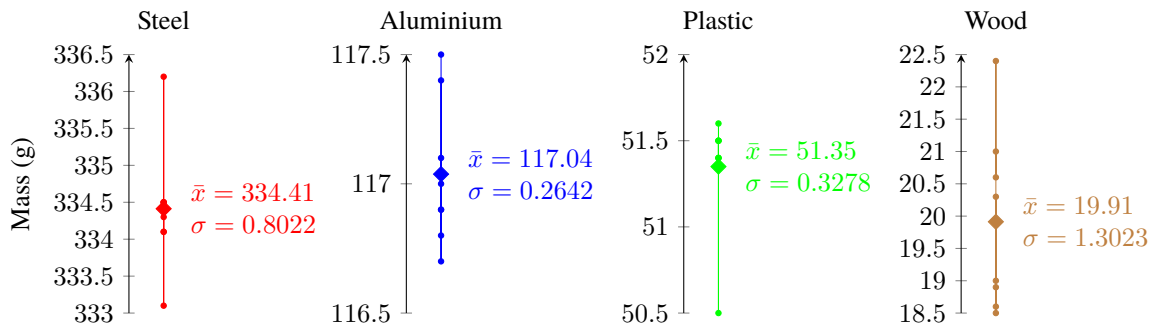


Figure 2.5: Masses for each set of eight 35 mm cubes of the configurable payload for each of the four materials, with the mean mass \bar{x} and standard deviation σ of each set.

Material	Variant	Density (kg m^{-3})
Wood	Pine	464.37
Plastic	Acrylic	1201.9
Aluminium	6082	2740
Steel	EN3B	7800

Table 2.1: The materials chosen for the cubes.

2.4 Results

2.4.1 Configuration Space

Given a $2 \times 2 \times 2$ matrix of cubes with the materials in table 2.1, there were a total of 65536 permutations, with a total mass range of $[0.38, 2.90]\text{kg}$, and a total COM range of $[-13.44, 13.44]\text{mm}$ on all axes. As some permutations mapped to the same point in configuration space, there were 62969 unique mass and COM vectors.

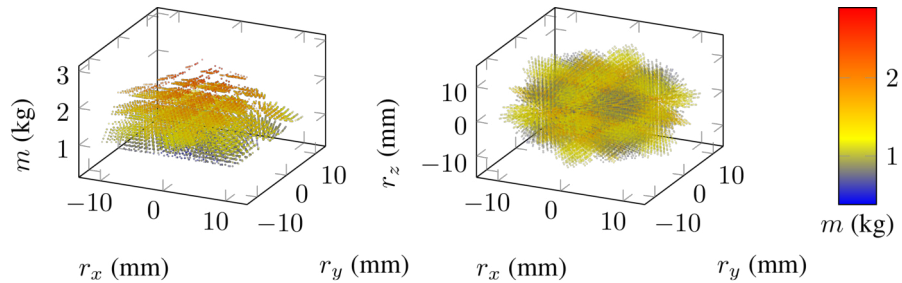


Figure 2.6: Scatter graph of all 62969 unique mass and COM vectors.

2.4.2 Test Points

The mass limit m_{max} for the extrema set was set at 1.25 kg, and the cube set length parameter b was set at 7 mm.

2.4.2.1 Mass and COM

m	r
Extrema Set (\mathcal{E})	
1.204	$[0.012 \quad 0.000 \quad -0.000]$
1.204	$[0.000 \quad 0.012 \quad -0.000]$
1.204	$[-0.012 \quad 0.000 \quad -0.000]$
1.204	$[0.000 \quad -0.012 \quad -0.000]$
0.380	$[0.000 \quad 0.000 \quad 0.000]$
1.009	$[0.011 \quad 0.011 \quad -0.000]$
1.009	$[-0.011 \quad -0.011 \quad 0.000]$
1.009	$[0.011 \quad -0.011 \quad 0.000]$
1.009	$[-0.011 \quad 0.011 \quad 0.000]$

Table 2.2: Table of the vectors of \mathcal{E} , excluding the mass-limited element.

Target			Nearest		L2 Norm Error
m	r	m	r		
Extrema Set (\mathcal{E})					
1.250	[0.000 0.000 *]	1.204	[0.000 0.000 -0.009]	4.556 $\times 10^{-2}$	
Cube Set (\mathcal{C})					
*	$[-0.007 \quad -0.007 \quad -0.007]$	0.987	$[-0.007 \quad -0.007 \quad -0.007]$	5.244 $\times 10^{-4}$	
*	$[-0.007 \quad -0.007 \quad 0.007]$	0.987	$[-0.007 \quad 0.007 \quad -0.007]$	2.023 $\times 10^{-2}$	
*	$[-0.007 \quad 0.007 \quad -0.007]$	0.987	$[0.007 \quad -0.007 \quad -0.007]$	2.023 $\times 10^{-2}$	
*	$[-0.007 \quad 0.007 \quad 0.007]$	0.987	$[0.007 \quad 0.007 \quad -0.007]$	2.023 $\times 10^{-2}$	
*	$[0.007 \quad -0.007 \quad -0.007]$	0.987	$[-0.007 \quad -0.007 \quad 0.007]$	2.023 $\times 10^{-2}$	
*	$[0.007 \quad -0.007 \quad 0.007]$	0.987	$[-0.007 \quad 0.007 \quad 0.007]$	2.023 $\times 10^{-2}$	
*	$[0.007 \quad 0.007 \quad -0.007]$	0.987	$[0.007 \quad -0.007 \quad 0.007]$	2.023 $\times 10^{-2}$	
*	$[0.007 \quad 0.007 \quad 0.007]$	0.987	$[0.007 \quad 0.007 \quad 0.007]$	5.244 $\times 10^{-4}$	
Balanced Set (\mathcal{B})					
0.598	[0.000 0.000 *]	0.575	[0.000 0.000 0.000]	2.229 $\times 10^{-2}$	
0.815	[0.000 0.000 *]	0.771	[0.000 0.000 -0.004]	4.459 $\times 10^{-2}$	
1.033	[0.000 0.000 *]	0.966	[0.000 0.000 0.000]	6.688 $\times 10^{-2}$	

Table 2.3: Table of the target and actual vectors for \mathcal{C} , \mathcal{B} and the mass limited element of \mathcal{E} with the L2 norm error. * notation indicates “don’t care” and is excluded from the search algorithm.

2.4.2.2 Material Permutations

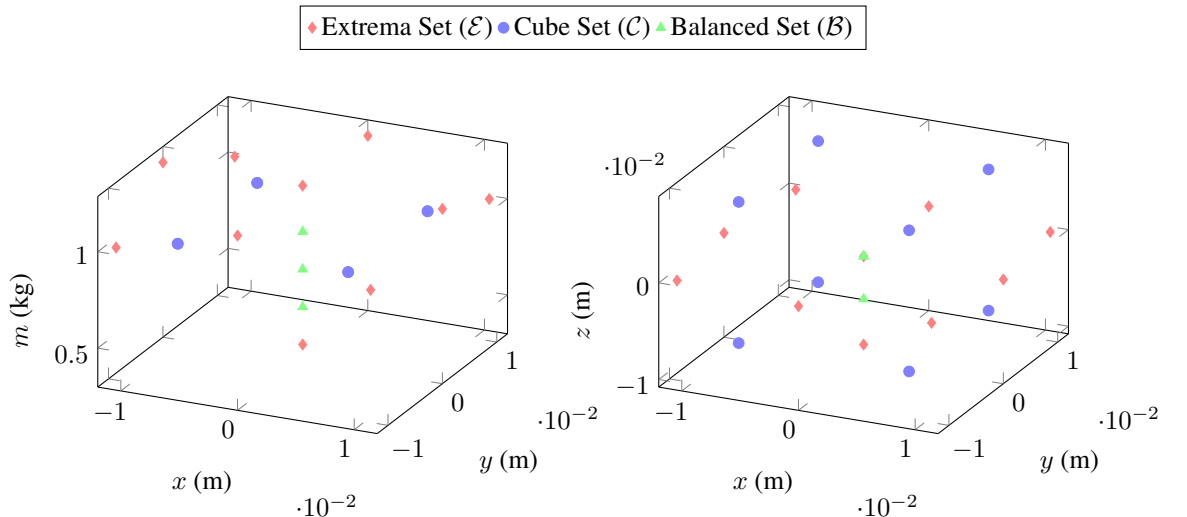


Figure 2.7: Mass and COM coordinates for each test point set.

m	r	Material Matrix		3D Preview
		Extrema Set (\mathcal{E})		
1.204	[0.000 0.000 -0.009]	$\begin{bmatrix} [S] & [A] \\ [W] & [S] \end{bmatrix} \quad \begin{bmatrix} [W] & [W] \\ [A] & [W] \end{bmatrix}$		
1.204	[0.012 0.000 -0.000]	$\begin{bmatrix} [W] & [W] \\ [S] & [A] \end{bmatrix} \quad \begin{bmatrix} [W] & [W] \\ [A] & [S] \end{bmatrix}$		
1.204	[0.000 0.012 -0.000]	$\begin{bmatrix} [W] & [S] \\ [W] & [A] \end{bmatrix} \quad \begin{bmatrix} [W] & [A] \\ [W] & [S] \end{bmatrix}$		
1.204	[-0.012 0.000 -0.000]	$\begin{bmatrix} [A] & [S] \\ [W] & [W] \end{bmatrix} \quad \begin{bmatrix} [S] & [A] \\ [W] & [W] \end{bmatrix}$		
1.204	[0.000 -0.012 -0.000]	$\begin{bmatrix} [A] & [W] \\ [S] & [W] \end{bmatrix} \quad \begin{bmatrix} [S] & [W] \\ [A] & [W] \end{bmatrix}$		
0.380	[0.000 0.000 0.000]	$\begin{bmatrix} [W] & [W] \\ [W] & [W] \end{bmatrix} \quad \begin{bmatrix} [W] & [W] \\ [W] & [W] \end{bmatrix}$		
1.009	[0.011 0.011 -0.000]	$\begin{bmatrix} [W] & [W] \\ [W] & [S] \end{bmatrix} \quad \begin{bmatrix} [W] & [W] \\ [W] & [S] \end{bmatrix}$		
1.009	[-0.011 -0.011 0.000]	$\begin{bmatrix} [S] & [W] \\ [W] & [W] \end{bmatrix} \quad \begin{bmatrix} [S] & [W] \\ [W] & [W] \end{bmatrix}$		
1.009	[0.011 -0.011 0.000]	$\begin{bmatrix} [W] & [W] \\ [S] & [W] \end{bmatrix} \quad \begin{bmatrix} [W] & [W] \\ [S] & [W] \end{bmatrix}$		
1.009	[-0.011 0.011 0.000]	$\begin{bmatrix} [W] & [S] \\ [W] & [W] \end{bmatrix} \quad \begin{bmatrix} [W] & [S] \\ [W] & [W] \end{bmatrix}$		

Table 2.4: Table of all test point configurations,

m	r	Material Matrix	3D Preview
Cube Set (\mathcal{C})			
0.987	$[-0.007 \quad -0.007 \quad -0.007]$	$\begin{bmatrix} [S] & [A] \\ [A] & [W] \end{bmatrix} \begin{bmatrix} [A] & [W] \\ [W] & [W] \end{bmatrix}$	
0.987	$[-0.007 \quad 0.007 \quad -0.007]$	$\begin{bmatrix} [A] & [S] \\ [W] & [A] \end{bmatrix} \begin{bmatrix} [W] & [A] \\ [W] & [W] \end{bmatrix}$	
0.987	$[0.007 \quad -0.007 \quad -0.007]$	$\begin{bmatrix} [A] & [W] \\ [S] & [A] \end{bmatrix} \begin{bmatrix} [W] & [W] \\ [A] & [W] \end{bmatrix}$	
0.987	$[0.007 \quad 0.007 \quad -0.007]$	$\begin{bmatrix} [W] & [A] \\ [A] & [S] \end{bmatrix} \begin{bmatrix} [W] & [W] \\ [W] & [A] \end{bmatrix}$	
0.987	$[-0.007 \quad -0.007 \quad 0.007]$	$\begin{bmatrix} [A] & [W] \\ [W] & [W] \end{bmatrix} \begin{bmatrix} [S] & [A] \\ [A] & [W] \end{bmatrix}$	
0.987	$[-0.007 \quad 0.007 \quad 0.007]$	$\begin{bmatrix} [W] & [A] \\ [W] & [W] \end{bmatrix} \begin{bmatrix} [A] & [S] \\ [W] & [A] \end{bmatrix}$	
0.987	$[0.007 \quad -0.007 \quad 0.007]$	$\begin{bmatrix} [W] & [W] \\ [A] & [W] \end{bmatrix} \begin{bmatrix} [A] & [W] \\ [S] & [A] \end{bmatrix}$	
0.987	$[0.007 \quad 0.007 \quad 0.007]$	$\begin{bmatrix} [W] & [W] \\ [W] & [A] \end{bmatrix} \begin{bmatrix} [W] & [A] \\ [A] & [S] \end{bmatrix}$	

Table 2.5

m	r	Material Matrix	3D Preview
Balanced Set (\mathcal{B})			
0.575	$[0.000 \quad 0.000 \quad 0.000]$	$\begin{bmatrix} [A] & [W] \\ [W] & [W] \end{bmatrix} \begin{bmatrix} [W] & [W] \\ [W] & [A] \end{bmatrix}$	
0.771	$[0.000 \quad 0.000 \quad -0.004]$	$\begin{bmatrix} [A] & [W] \\ [A] & [A] \end{bmatrix} \begin{bmatrix} [W] & [A] \\ [W] & [W] \end{bmatrix}$	
0.966	$[0.000 \quad 0.000 \quad 0.000]$	$\begin{bmatrix} [A] & [A] \\ [W] & [A] \end{bmatrix} \begin{bmatrix} [A] & [W] \\ [A] & [A] \end{bmatrix}$	

Table 2.6

2.5 Discussion & Conclusion

2.5.1 Future Work

2.5.1.1 Payload with Improved COM Range

As mentioned in 2.4.1, the COM range of the configurable payload is very small. Similarly to the mass range, the COM range could be increased by the use of denser and lighter materials. However, with the current design, it is not possible to increase the COM range by a significant amount. This is due to the small offset distance of the COM of each material cube, only 17.5 mm from the geometric centroid of the payload. A design that could increase the maximum offset distance would therefore increase the COM range significantly. One proposal would be to use a rod with a mass on one end and a handle for the grippers on the other. The mass material, thickness, and length of the rod could then be varied to adjust the mass and COM of the payload. Since the gripper can rotate 360° with the chosen robot arm, any COM can be simulated within a annulus shaped configuration space around $z = 0$ for a given mass, but could be extruded to an annular cylinder if some mechanism was used to vary the z element of the COM (asymmetric masses, rod sliders on the handle, etc.). If two rods either side of the handle are used, the annuli become disks and cylinders respectively, allowing for “balanced” payloads, as can be seen in figure 2.8. This is an advantage over the original design, and eliminates the need for any kind of search algorithm for the COM, since it could be found analytically for a given mass using polar coordinates, where the *radius* is the rod length and the *azimuth* is the gripper rotation angle, though it must be noted the mass and maximum rod length will determine the available range of values for the COM.

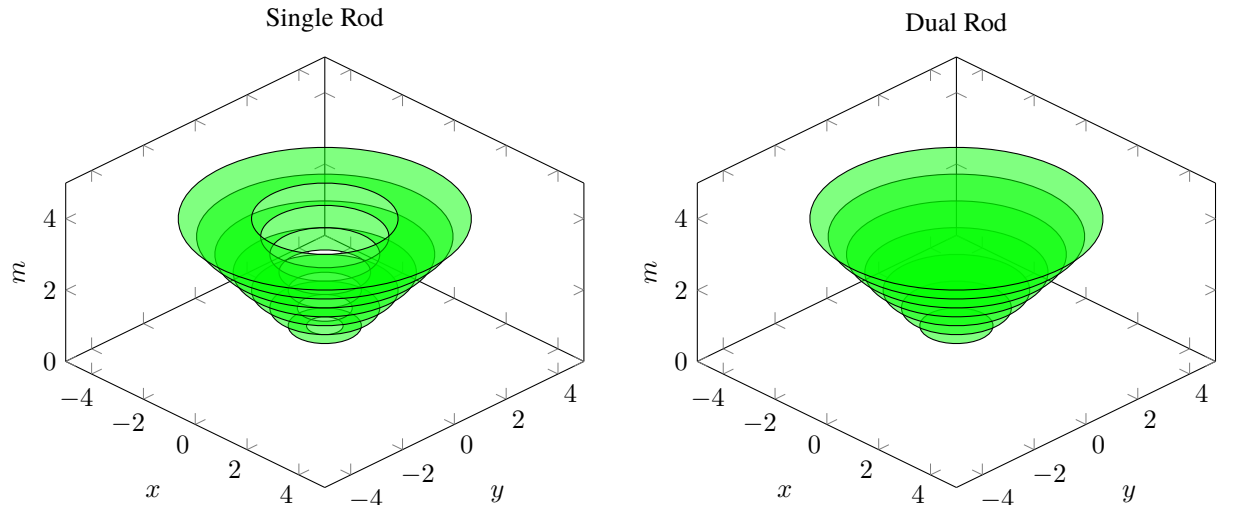


Figure 2.8: Example configuration space for the new configurable payload design, where $z = 0$.

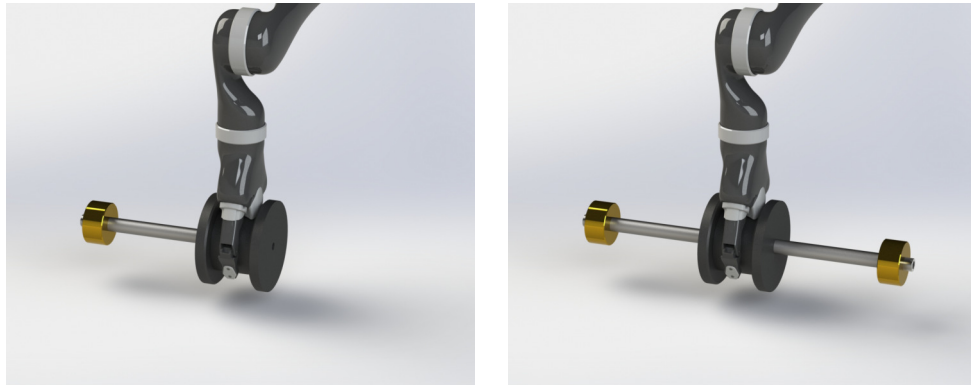


Figure 2.9: Renders of a concept design for the new configurable payload, with a single rod and dual rod configuration.

2.5.1.2 Dynamic COM Implementation: Fluid Filled Container

Not all payloads that a robot may pick up are solid objects, some may have COM that shift during transit due to external disturbances. Generally any container partially filled with either loose material or fluid, such as a bottle or sack, could have a so-called “dynamic” COM. Therefore, a container partially filled with fluid, with a specific viscosity and mass would be a suitable simulacrum for these kinds of payloads. The robot arm could then shake the container from side to side briefly to simulate a disturbance, creating a standing wave inside the container that would have an effect on the COM.

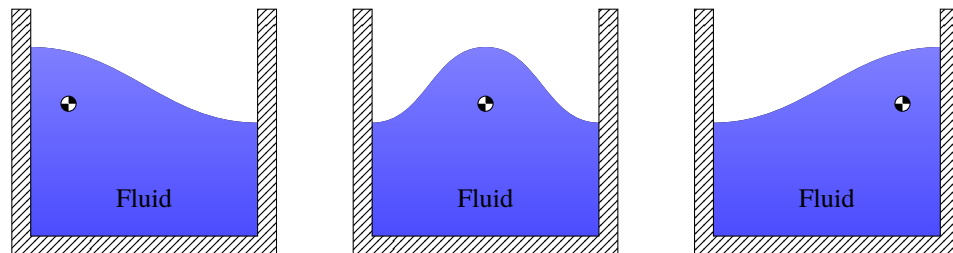


Figure 2.10: Diagram on the COM dynamics of a fluid filled container. If the container is disturbed, a standing wave forms inside the container which causes the COM to oscillate.

2.5.2 Conclusion

This work has outlined the design and implementation of a configurable payload that is suitable for the experiments in chapter ???. Using this payload, a range of objects with different mass and COM can be emulated in order to generate a wide range of experimental data.

References

- [1] *Kinova mico™ robotic arm 4dof specifications*, 1.2, Kinova, Inc., Apr. 2018.
[Online]. Available: <https://drive.google.com/file/d/1xCmpqSDMZvKU4IypSaXBLIEX6p7pigGr/view>.

- [2] S. Kirkpatrick, C. D. Gelatt, and M. P. Vecchi, “Optimization by simulated annealing,” *science*, vol. 220, no. 4598, pp. 671–680, 1983.
- [3] P. Serafini, “Simulated annealing for multi objective optimization problems,” in *Multiple criteria decision making*, Springer, 1994, pp. 283–292.

Chapter 3

Investigating the use of a 2DOF Pendulum Tail for Compensating for Instability when Carrying a Payload

3.1 Introduction

As mentioned in chapter ??, the primary question of this research is to quantify the efficacy of a robotic tail for maintaining the stability of a mobile robot when carrying a payload.

While the ultimate verification for this question would be to attach a tail to a mobile robot and engage in field trials, carrying objects in a close simulacrum to a real operating environment, a simpler and more flexible approach is to use a static rig which can measure a “virtual” static stability using the COP. By comparing the measurement to a robot’s known stability region (typically referred to as the *support polygon*[1]) and initial center of mass, it is possible to determine if a specific mobile robot would remain statically stable without having to topple a mobile robot, and risk equipment damage.

However, demonstrating an improvement in a discrete set of pass/fail stability tests based on specific mobile robots is not necessary to answer the research question. Instead, a continuous approach can be used, which considers stability as a cost function rather than a binary result. This has the advantage of being able to quantify *how* stable the experiment is, and the magnitude of dynamic forces a given robot could withstand. The smaller the cost and the larger the support polygon, the greater the magnitude, depending on the distance to the polygon boundary in a specific direction.

3.1.1 Chapter Summary

In this chapter, the design of the static rig is outlined, made up of a base, a robotic arm, the configurable payload from chapter 2, a 2 DOF “inverted pendulum” tail driven by two brushless motors using a bevel gear arrangement, and four load cells used to calculate the COP. N cost functions for stability are then derived from the COP data when the payload is being lifted by the arm. An experimental trajectory is described which replicates the motions of a mobile robot moving and object from one location to another. A simple propor-

tional controller is then developed and simulated, and its efficacy is compared with experimental results from the constructed rig for each test point set in chapter 2. The discussion then examines the efficacy of the chosen design and actuation method for the robotic tail, and its limitations and potential improvements, as well as examining the ability of the configurable payload to generate a suitably wide range of test points, given the variation in the motion of the tail for each point.

3.2 Experiment Design

The static rig can be abstractly defined as follows: a rectangular base of dimensions $\begin{bmatrix} b_x & b_y \end{bmatrix}$ centred around the origin where the force is measured at each vertex to create a matrix $\mathbf{F} \in \mathbb{R}^{2 \times 2}$ where each element is the force measured at the corner of the rectangle defined by its position in the matrix. The robot arm and tail are positioned along the origin X axis at a_y and $-t_y$ on the Y axis, and a_z and t_z on the Z axis. The tail is a rod attached to a 2 DOF joint, with the orientation controlled by input angles θ . The robot arm is a 4 DOF design with a pair of grippers to pick up a payload, with the input angles \mathbf{q} .

\mathbf{F} can then be used to measure the Center of Pressure, defined as the the point of application of the GRF vector. [2] gives the following equation to calculate the COP:

$$\mathbf{F} = \begin{bmatrix} f_{x,y} & f_{-x,y} \\ f_{x,-y} & f_{-x,-y} \end{bmatrix}$$

$$CP(\mathbf{F}) = \begin{bmatrix} \frac{b_x ((f_{11} + f_{21}) - (f_{12} + f_{22}))}{\sum_{i=1}^2 \sum_{j=1}^2 f_{ij}} \\ \frac{b_y ((f_{11} + f_{12}) - (f_{21} + f_{22}))}{\sum_{i=1}^2 \sum_{j=1}^2 f_{ij}} \end{bmatrix} \quad (3.1)$$

Where $f_{\square,\square}$ refers to the location of the load measurement on figure 3.1.

Four load cells were used instead of a force plate, which would have likely resulted in a more accurate measurement, in order to replicate what would be practical to measure on a mobile robot. Attaching load cells to each leg or wheel mount on a mobile robot would be fairly trivial and cost effective, dividing the body in order to insert a force plate or dynamometer would be difficult ad costly. [2], [3] compare a similar mechanism using the Wii Fit™ Balance Board, and was able to achieve a COP repeatability to within 1.5 mm.

$$CP(\mathbf{F}) = \frac{m_b \mathbf{r}_b + m_a \mathbf{r}_a(\mathbf{q}) + m_p \mathbf{r}_p(\mathbf{q}) + m_t \begin{bmatrix} l_t \cos \theta_1 \\ -t_y + l_t \cos \theta_2 \end{bmatrix}}{m_b + m_a + m_t} \quad (3.2)$$

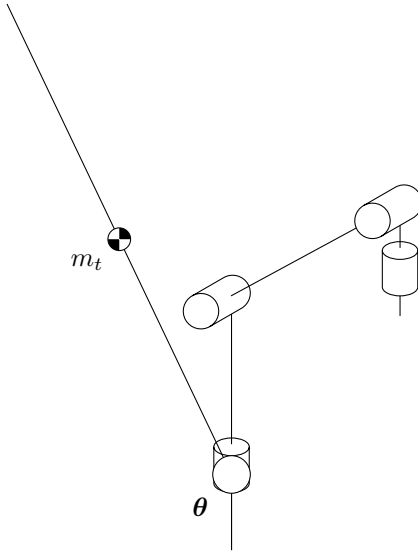


Figure 3.1: Free body diagram of the static test setup.

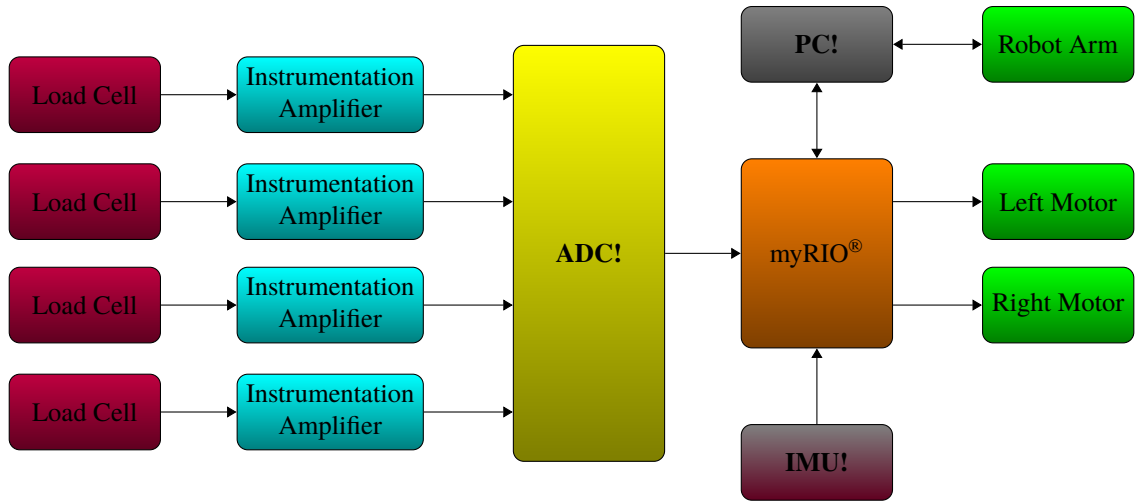


Figure 3.2: System diagram of the static rig.

3.2.1 Base

The base consists of two pairs of steel plates orthogonal to each other, separated by load cells and rubber vibration dampers. The lower plates are clamped to a sturdy table at the four positions indicated in figure 3.3, and a pair of shallow Unistrut[®] channels are bolted between the upper plates. The plates for the robot arm and tail are then secured to the rig with nuts that slot into the channels, allowing them to be shifted along the Y axis so a_y and t_y can be adjusted.

The load cells are OmegaTM LCM204 with a range of $\pm N$, connected to Fylde FE-359-TA instrumentation amplifiers that fed the amplified signal to an Analog Devices AD7606 Analog to Digital Converter (ADC), which was connected to the National Instruments (NI) myRIO[®]. A separate ADC was chosen due the limited number of differential analog inputs on the myRIO[®], with only two on the MSP connector [4]. The chosen ADC also had a greater resolution of 16 bits [5] than the built-in myRIO[®] ADC of 12 bits [4].

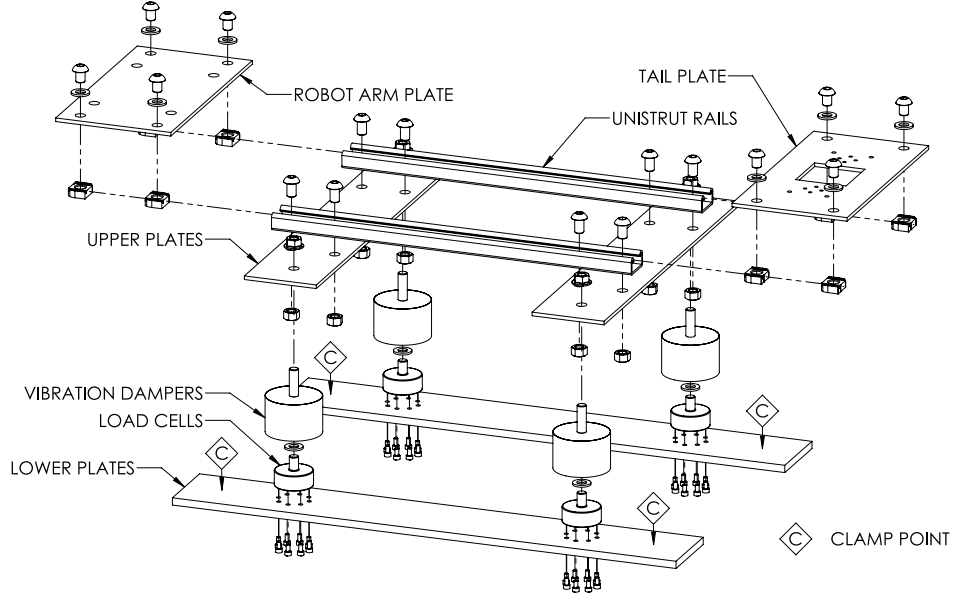


Figure 3.3: Exploded schematic of the base of the static rig, with important components labelled and clamping points marked.

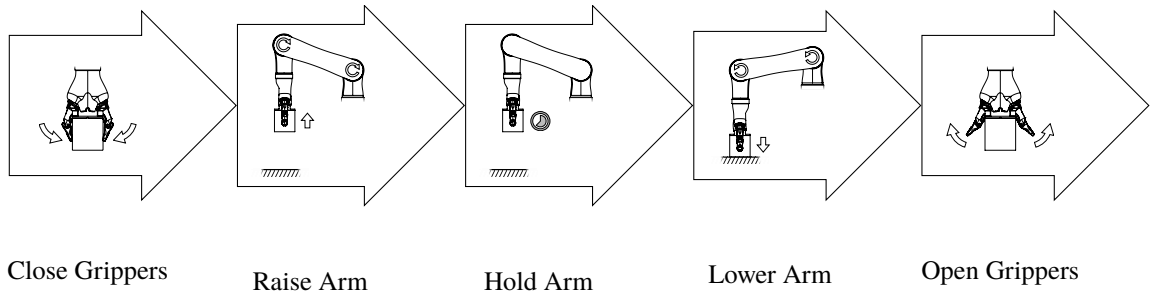


Figure 3.4: Trajectory sequence of the robot arm and payload.

3.2.2 Robot Arm

3.2.3 2 DOF Tail

3.2.4 Trajectory

The experimental trajectory is designed to replicate the actions of a mobile robot that is moving an object from one place to another. The robot arm grasps the payload and lifts it off the ground plane, then holds it for a predetermined period of time, before placing it back down on the ground plane and releasing it.

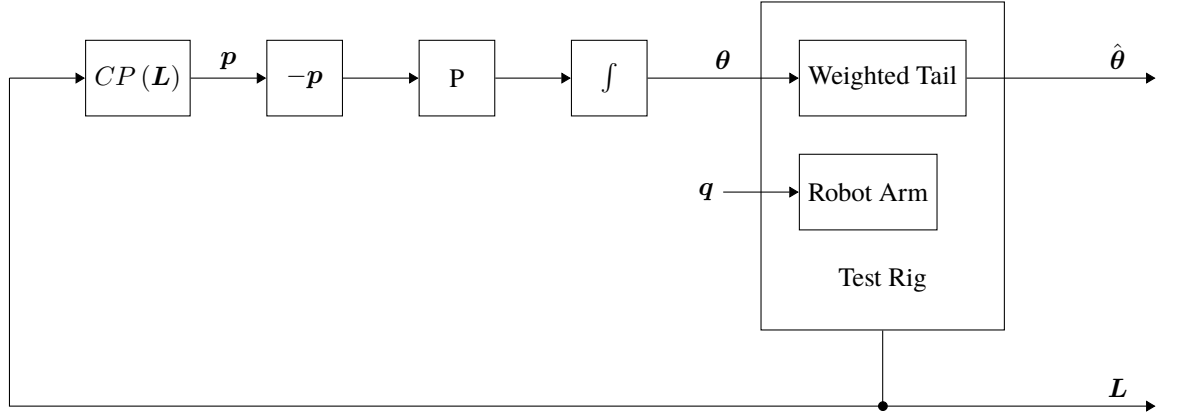


Figure 3.5: Simulation block diagram.

3.3 Simulation

3.3.0.1 Control System

3.4 Experiments

3.4.1 Design

In order to save time and maintain payload alignment between runs and test points, the arm remains close to the payload once it has been set down. Since the grippers are open, the payload does not influence the COP during this time.

3.4.1.1 Control System

$$\begin{aligned} \mathbf{F} &= \begin{bmatrix} f_{x,y} & f_{-x,y} \\ f_{x,-y} & f_{-x,-y} \end{bmatrix} \\ CP(\mathbf{F}) &= \begin{bmatrix} \frac{l_x((f_{11} + f_{21}) - (f_{12} + f_{22}))}{\sum_{i=1}^2 \sum_{j=1}^2 f_{ij}} \\ \frac{l_y((f_{11} + f_{12}) - (f_{21} + f_{22}))}{\sum_{i=1}^2 \sum_{j=1}^2 f_{ij}} \end{bmatrix} \end{aligned} \quad (3.3)$$

Equation from [6]:

$$\dot{\phi} = \begin{bmatrix} 1 & -1 \\ -1 & -1 \end{bmatrix} \dot{\theta} \quad (3.4)$$

3.4.2 Results & Performance

For each test point, 20 experiments were run, 10 *control* experiments without the tail attached, and 10 *tail* experiments with the feedback controlled tail. The mean values for the

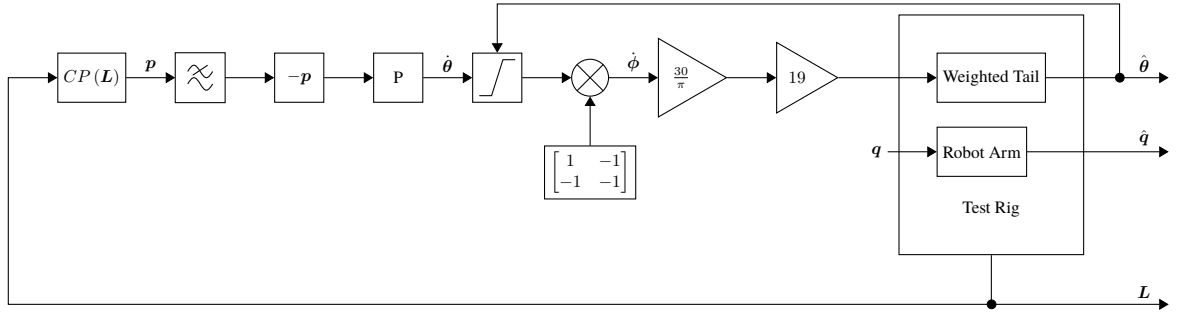


Figure 3.6: Block diagram of the control system.

10 experiments were then taken as the performance measurements, with the minimum and maximum values considered as the measurement error.

In order to provide a fair comparison between the control and tail experiments, a perfectly balanced initial condition is assumed for the control experiments. This was done by offsetting the COP data by the value of the initial condition.

The following data was taken from each run of the experiment, where each symbol represents a scalar or vector time series $\{x_t; t \in \mathbb{R}^+ | t \leq n\}$ where n is the final sample time:

3.4.2.1 Center of Pressure

One option is to measure the minimum

This point may not exist within the time series

3.4.2.2 Vibration Analysis

3.4.2.3 Payload & Tail Angle Regression Analysis

To examine the effects of varying the payload mass and COM on the tail, a regression study was conducted comparing mass and COM *inputs* to tail angle *outputs*, specifically the peak angle output measured by the maximum magnitude function, where θ represents the vector of tail angle measurements from the experiment:

$$\wedge(\theta) = \begin{cases} \max \theta & |\max \theta| \leq |\min \theta| \\ \min \theta & |\max \theta| > |\min \theta| \end{cases} \quad (3.5)$$

Figure ?? shows the correlations between the maximum magnitude of the tail on both pitch and roll axes, and the mass and corresponding COM of the payload. A change in the x axis of the COM would only affect the roll, and the y axis would only affect the pitch, but a change in mass would effect both, though the y axis to a much greater degree.

The results show that there is a strong correlation ($p = 6.858 \times 10^{-13}$) between the payload mass and the pitch maximum magnitude of the tail of $1.045 \text{ rad kg}^{-1}$. There are also weaker

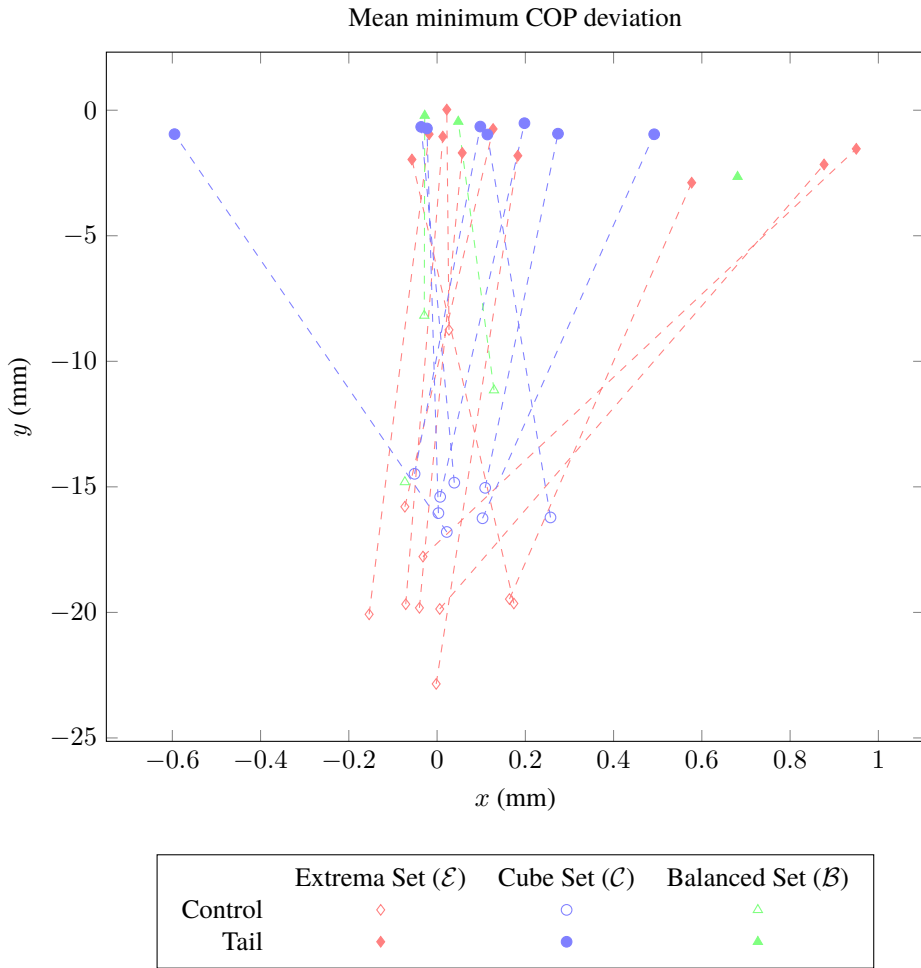


Figure 3.7: Graph of the mean COP during the *carry* phase of the experiment

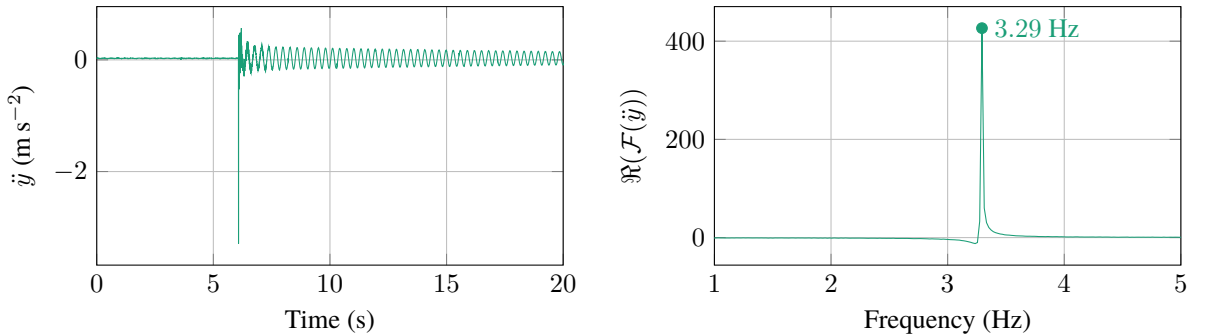


Figure 3.8: Resonant frequency of the tail calculated from accelerometer data captured during an impact with a steel hammer. The left graph is the accelerometer data, and the right graph is the real part from a real DFT on the data.

correlations ($p = 0.598$ and $p = 0.082$) between the COM x and y axis and the pitch maximum magnitude of the tail at 0 rad mm^{-1} and 0 rad mm^{-1} respectively. While these are too large to be considered a statistical certainty ($p > 0.05$), they do still suggest a approximately 90% probability there was an effect, assuming the mean values from each test point are accurate.

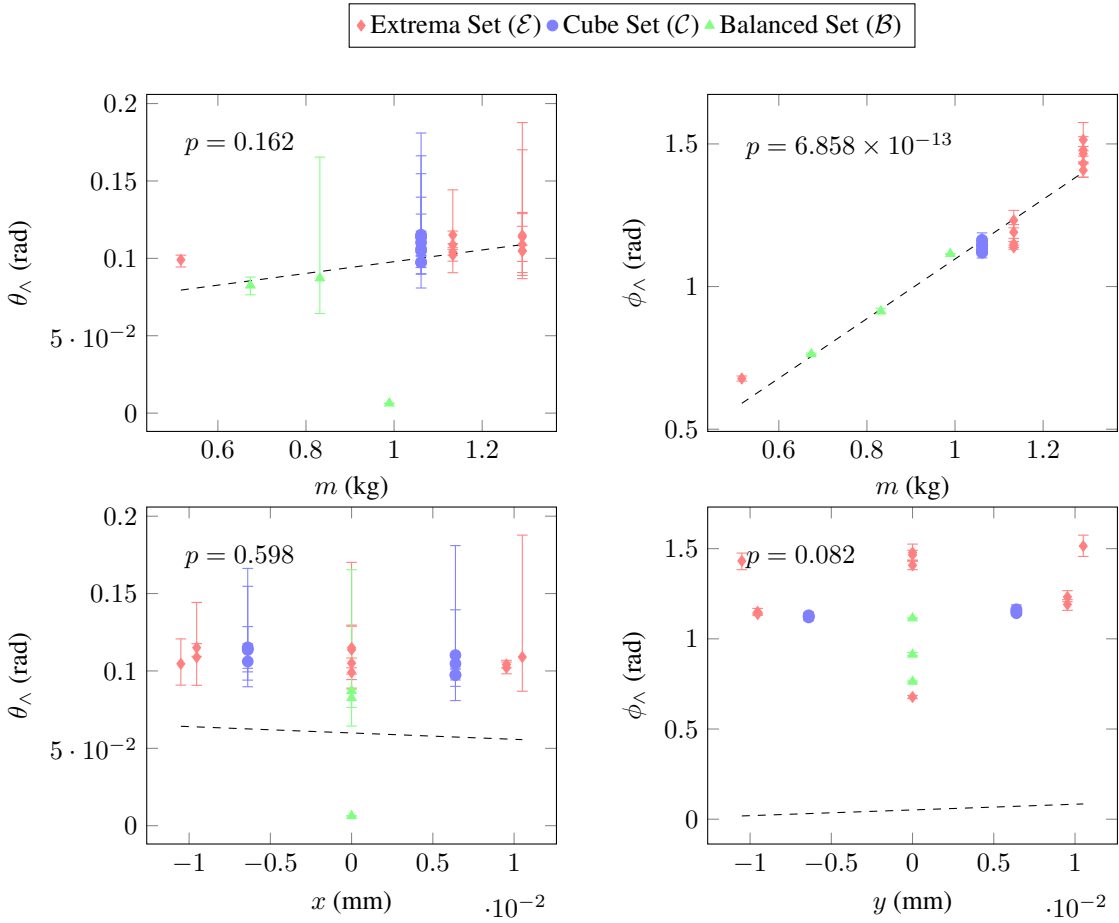


Figure 3.9

3.5 Discussion and Conclusion

A major issue with the experiments that likely prevented the collection of more accurate data and more stable control of the tail was the vibration of the tail shaft. This could potentially be alleviated by using a stiffer material for the shaft, or using a shaft of a larger diameter. However, this would likely increase the mass of the tail shaft, or would require more specialised materials to be sought.

References

- [1] R. B. McGhee and A. A. Frank, “On the stability properties of quadruped creeping gaits,” *Mathematical Biosciences*, vol. 3, pp. 331–351, 1968.
- [2] H. L. Bartlett, L. H. Ting, and J. T. Bingham, “Accuracy of force and center of pressure measures of the wii balance board,” *Gait & posture*, vol. 39, no. 1, pp. 224–228, 2014.
- [3] J. M. Leach, M. Mancini, R. J. Peterka, T. L. Hayes, and F. B. Horak, “Validating and calibrating the nintendo wii balance board to derive reliable center of pressure measures,” *Sensors*, vol. 14, no. 10, pp. 18 244–18 267, 2014.

- [4] *NI myRIO-1900 user guide and specifications*, National Instruments, May 2016.
- [5] *AD7606/AD7606-6/AD7606-4 data sheet*, version F, Analog Devices, Apr. 2020.
- [6] A. Patel and E. Boje, “On the conical motion of a two-degree-of-freedom tail inspired by the cheetah,”
IEEE Transactions on Robotics, vol. 31, no. 6, pp. 1555–1560, 2015.
doi: 10.1109/TRO.2015.2495004.

Appendices